Two-fluid simulations of an aerated lab-scale bioreactor

Jamshidian, Roya; Scully, James; Van den Akker, Harry E.A.

DOI
10.1016/j.cherd.2023.06.042

Publication date
2023

Document Version
Final published version

Published in
Chemical Engineering Research and Design

Available online at www.sciencedirect.com

Chemical Engineering Research and Design

journal homepage: www.elsevier.com/locate/cherd

Two-fluid simulations of an aerated lab-scale bioreactor

Roya Jamshidian[a], James Scully[d], Harry E.A. Van den Akker[a,b,c,*]

[a] Synthesis and Solid-State Pharmaceutical Centre (SSPC), University of Limerick, V94 T9PX Limerick, Ireland
[b] Bernal Institute & School of Engineering, University of Limerick, V94 T9PX Limerick, Ireland
[c] Department of Chemical Engineering, Delft University of Technology, Van der Maasweg 9, 2629 HZ Delft, the Netherlands
[d] Regeneron Ireland DAC, Raheen Business Park, Limerick, Ireland

ARTICLE INFO

Article history:
Received 23 March 2023
Received in revised form 20 June 2023
Accepted 20 June 2023
Available online 22 June 2023

Keywords:
Impeller
Sliding mesh
Air headspace
Multiple reference frame
Computational mesh
Spurious vectors

ABSTRACT

We report the findings of a detailed assessment of various options for computational two-fluid RANS simulations of an aerated agitated 2-L bioreactor equipped with a single baffle and several dip tubes. The simulations were carried out by using the commercial flow solver ANSYS/Fluent. Our focus was on (1) the outlet condition at the liquid's surface (*i.e.*, including an air head space in the simulation yes or no); (2) the choice between the steady-state Multiple Reference Frames (MRF) approach for modelling the impeller rotation and the dynamic Sliding Mesh (SM) option; (3) the choice between two computational meshes (mosaic or polyhedral); and (4) the effect of using either the realizable k-ε model or the SST k-ω model for dealing with the turbulence in combination with different values for the fixed bubble size (either 1.8 or 2.8 mm). The final conclusion is that the SM impeller model in combination with a polyhedral computational mesh and the SST k-ω turbulence model is to be preferred. All simulations suffer from the occurrence of spurious velocities larger than the impeller tip velocity.

1. Introduction

1.1. *Preamble*

In the several decades of his impressive and productive career in the discipline of mixing, the late Professor Alvin Nienow studied various sub-fields, such as solids suspension, gas dispersion, emulsions, and micro-mixing. Without downplaying the significance of Alvin's earlier papers in these sub-fields, his most impressive contributions may have been in the field of bioprocessing. He greatly improved our understanding of particularly the scale-up of aerated agitated vessels and cell damage in agitated bioreactors. An illustrative example of the latter is Alvin's 2006 paper (Nienow, 2006) which discusses many aspects of animal cell cultures in bioreactors ranging from 2 L lab scale all the way up to 10 kL production scale.

Over the years, Alvin also got more and more interested in the performance of (preferably agitated) lab-scale reactors. Two 2013 papers, in *Biotechnology Letters* (Rafiq et al., 2013) and in *Biochemical Engineering Journal* (Nienow et al., 2013), report on the health and productivity of cell cultures in both a 5 L bioreactor and an agitated 15 mL vessel. Even very recently, Alvin was co-author of a paper on the first successful use of an agitated 5 L bioreactor for growing human mesenchymal stem cells on micro-carriers (Rotondi et al., 2021).

While most of Alvin's work strongly leaned on experiments, several of his papers also comprise findings obtained by means of Computational Fluid Dynamics (CFD), such as (Oshinowo et al., 2000), Jaworski et al. (Jaworski et al., 2000), and Bujalski

* Corresponding author at: Bernal Institute & School of Engineering, University of Limerick, V94 T9PX Limerick, Ireland.
E-mail address: Harry.VanDenAkker@ul.ie (H.E.A. Van den Akker).
https://doi.org/10.1016/j.cherd.2023.06.042

Nomenclature

C_D	Drag coefficient.
d_O	Sparger orifice diameter (m).
d_B	Bubble diameter (m).
D	Impeller diameter (m).
F_D	Drag force (N).
g	Gravitational acceleration ($m.s^{-2}$).
G_k	TKE generation due to mean velocity gradients.
G_ω	Generation of ω.
H	Liquid height (m).
k	Turbulent kinetic energy.
N	Rotational speed (rpm).
N_P	Power number.
p	Pressure ($N.m^{-2}$).
P_u	Power input without gassing, (W).
P_T	Power input calculated from torque (W).
P_ε	Power dissipation due to turbulent dissipation (W).
Re	Reynolds number.
S	Strain rate tensor (s^{-1}).
t	Time (s).
T	Tank diameter (m).
u	Velocity ($m.s^{-1}$).
u_{tip}	Blade tip velocity ($m.s^{-1}$).
Y_k	Dissipation of k due to turbulence.
Y_ω	Dissipation of ω due to turbulence.

Greek symbols

α_m	Volume fraction of phase m.
ε	Turbulent energy dissipation rate ($m^2.s^{-3}$).
μ_L	Liquid viscosity (Ns/m^2).
μ_t	Turbulent viscosity of liquid (Ns/m^2).
ν_L	Kinematic viscosity ($m^2.s^{-1}$).
ρ_m	Density of phase m ($kg.m^{-3}$).
σ	Surface tension ($N.m^{-1}$).
σ_k, σ_ε	Turbulent Prandtl numbers.
τ_m	Turbulent stress in phase m.

Abbreviations

BC	Boundary condition.
MRF	Multiple Reference Frames.
RPM	Rotations per minute.
SM	Sliding Mesh.
TKE	Turbulent kinetic energy.

et al. (Bujalski et al., 2002). In this contribution to this special issue of *Chemical Engineering Research and Design* in memory of Alvin, we report on CFD simulations of an aerated lab-scale bioreactor, typically in the 2–5 L range. We have opted for the two-fluid (or Euler-Euler) modelling approach in which both the liquid carrier phase and the bubbles (the dispersed phase) are considered as interpenetrating continua. This focus on the flow behaviour of the two phases implies that we refrain from resolving the motion of individual bubbles. We further assume that the flow in our lab-scale bioreactor is turbulent, given Re= 14,925. Since hardly any experimental data are available for validating our simulation, our simulations should primarily be interpreted as a sensitivity study.

1.2. *Background of the study*

The idea behind the study reported in this paper was that – certainly over the course of Alvin's professional career – CFD has grown into a rather mature technique that often delivers insights about the internal flow within a device not easily attainable by experimental techniques. Companies are increasingly inclined to accept and rely on results from CFD studies without an extensive validation by experimental data, certainly in cases where experimental facilities are not readily available or not capable of acquiring the detailed information of interest. This even applies to such basic information as the Power Number of single-phase lab-scale reactors about which Zeinali et al. reported on the North American Mixing Forum (NAMF) Mixing XXVII meeting in 2022.

The challenging question addressed here is whether two-fluid CFD has also sufficiently advanced such that lab-scale bioreactors can be simulated with a decent degree of confidence. To the best of our knowledge, just a few journal papers deal with two-fluid CFD simulations of lab-scale reactors. Now, our paper focuses on elementary aspects (impeller treatment, mesh type, and turbulence model) in performing two-fluid simulations for an aerated 2 L reactor with a central impeller and several inserts. A topic of particular interest relates to the treatment of the moving impeller in such a lab-scale reactor: should we favour the transient Sliding mesh (SM) model or does the steady-state Multiple Reference Frames (MRF) approach (equally) adequate results? As a result, our sensitivity study may be welcomed as a useful contribution and extension to the state of the art. A special aspect of our paper, usually not reported in other papers, is the attention paid to the frequent occurrence of large velocity vectors, which were identified as spurious velocities.

A detailed review of the state of the art in computationally simulating gas-liquid mixing in stirred vessels by means of RANS-type two-fluid models is beyond the scope of this paper. The reader is referred to earlier reviews (Kerdouss et al., 2006; Sajjadi et al., 2012; Shi and Rzehak, 2018). Of course, all insights acquired in single-phase flow simulations about the effects of turbulence models, numerical schemes, and mesh sizes (Aubin et al., 2004; Haringa et al., 2018b; Joshi et al., 2011a, b; Karimi et al., 2012a; Karimi et al., 2012b); Haringa et al., 2018b) are very relevant as well. More recently, the Delft PhD theses of Günyol (Günyol, 2017) and Haringa (Haringa, 2017) present detailed assessments of all these effects as well as of bubble size in the context of multiple-impeller fermenters. Kerdouss et al. (Kerdouss et al., 2008) and (Bach et al., 2017) carried out two-fluid simulations to study mass transfer in bioreactors.

The use of population balances supported by various models for bubble break-up and coalescence was investigated by *e.g.* (Venneker et al., 2002) and (Kerdouss et al., 2008). (Sajjadi et al., 2012) even identified bubble size distribution as the most important parameter in bioreactors. Several authors validated two-fluid simulations for aerated stirred vessels by means of experimental data (Kerdouss et al., 2008; Montante et al., 2007). The review paper by (Dhotre et al., 2013) on large eddy simulations of dispersed bubbly flows in bubble columns also presents a wealth of

information relevant to two-fluid simulations of aerated stirred vessels.

To the best of our knowledge, just a few journal papers deal with two-fluid CFD simulations of lab-scale reactors. (Cappello et al., 2021) studied upscaling of aerated bioreactors starting at a 20 L vessel. (Li et al., 2018) performed two-fluid simulations in 15 mL and 250 mL aerated bioreactors and concluded, among other things, that, compared to MRF, an SM scheme is superior in reactors with asymmetric geometries where the sparger is not positioned in the centre. A somewhat similar conclusion was reported by (Sadino-Riquelme et al., 2022) for a 4 L vessel when flow instabilities played a role.

1.3. *The challenges of a lab-scale bioreactor*

First of all, most lab-scale bioreactors do not contain wall-mounted baffles; instead, they typically have an eccentrically positioned single baffle, often of the beaver-tail type. The small size of the vessel implies that the impeller, baffle, aeration device, and often several dip tubes are in very close proximity to each other. As a result, the flow behaviour is very complex, not only because a (precessing) vortex may be formed, but also because the flow structures (wakes, vortices) around all these inserts may interact. It is unclear whether the turbulence may be classified as sufficiently isotropic to allow for the use of a k-ε model and whether the turbulence spectrum is fully developed and can be described in terms of the well-known −5/3 slope encompassing some decades. (Newell and Grano, 2007) refer to (Schubert, 1986) who reported that turbulence is not fully developed in flotation cells (with a Rushton turbine) smaller in volume than 30 L. It may also not be very clear how bubbles respond to the close proximity of all the inserts and their flow structures. Blindly relying on all CFD expertise collected in large-scale vessels may therefore not be a good idea when simulating lab-scale bioreactors.

One of the aspects deserving special attention when simulating lab-scale bioreactors relates to the treatment of the revolving impeller for which two options are available. In both options, the flow domain is divided into an inner zone encompassing the revolving impeller and an outer stationary zone connected to the vessel walls (and the baffles). The rule of thumb as to where to choose the boundary between the two zones is that it is as remote from the impeller and baffles as possible. In large vessels, this is easy to accomplish. Most reports in the literature (Ammar et al., 2011; Karimi et al., 2012a; Kerdouss et al., 2008; Lane et al., 2000a, b) then conclude that the steady-state MRF approach is sufficiently accurate at a much more economical computational time. In a lab-scale bioreactor, however, choosing the boundary between the 'revolving' inner domain and the stationary outer domain in both the MRF and the SM approaches is very challenging. The same applies to generating a satisfactory mesh that properly accommodates the close proximity of all internals and their combined effect on the flow field. The question is whether all lessons learned at larger scales are relevant and valid in lab-scale vessels.

Given all the uncertainties and issues mentioned above, this paper reports about a sensitivity study exploring four major aspects of two-fluid simulations of a lab-scale bioreactor:

- The possibility of a (precessing) vortex at the liquid surface: do we need to include the air head space above the agitated liquid with the usual pressure outlet condition or is it sufficient to only consider the liquid phase, without a headspace, and to use a so-called degassing condition as recommended by (Günyol, 2017)?
- The dilemma of using either the steady-state and faster MRF approach for dealing with the revolving impeller or the more time-consuming dynamic SM technique.
- The effect of using various mesh types for discretizing the flow domain, more specifically Fluent's mosaic mesh or a straightforward polyhedral mesh.
- The (combined) effect of using different turbulence models (either the realizable k-ε model or the SST k-ω model) and a different value for the fixed bubble size (either 1.8 or 2.8 mm).

A separate issue is the occurrence of so-called spurious velocity vectors in many of our numerical simulations: these spurious vectors are numerical artifacts as a result of inaccuracies in the numerical computations and/or mismatches between flow direction, domain geometry, and computational mesh.

The remainder of the paper is organized as follows: first, in chapter 2, the equations and models used will be summarized. Then, in chapter 3, the details of the computational approach will be presented. In chapter 4, the results of investigating the four above aspects will be reported, followed by a discussion in chapter 5. The conclusions of our sensitivity study are then communicated in chapter 6.

2. Modeling approach

2.1. *Modeling the flow field*

In the current study, a two-fluid or Euler-Euler approach is being used to simulate the two-phase domain of a 2 L lab-scale stirred bioreactor under turbulent-flow conditions. The software used for carrying out the simulations is Fluent 2022R2 (ANSYS Inc, Canonsburg, PA 15317, USA). In the two-fluid method, the two phases are conceived as interpenetrating continua such that the continuity and momentum equations for each phase are solved simultaneously.

The mass and momentum conservation equations are displayed in Table 1 (Eq. 1 and equation 2, respectively) and the subscript m is a representation of the phase which can be replaced with l for the liquid and g for the gas phase. The last term on the right-hand side of equation (2) indicates the interphase forces between the two phases. Previous studies (Lane et al., 2002; Sanyal et al., 1999; Scargiali et al., 2007) have shown that the influence of all interphase forces (such as lift force and virtual mass) apart from the drag force (F_D) is largely negligible in the simulation of a stirred bioreactor. Therefore, in the current study, only the drag force is taken into account with an imposed constant bubble diameter. Coalescence and break-up of bubbles are not considered, mainly due to the (very) low aeration rates.

In most cases of our study, the air headspace above the liquid is part of the flow domain, with the air bubbles being injected at the bottom of the tank which is half-filled with the liquid. For such cases, in which the dispersed phase in one domain becomes the continuous phase in the other, Fluent's so-called symmetric drag model (Eq. 3) is used.

Two Reynolds Averaged Navier-Stokes (RANS) models are used to model the turbulent flow inside the bioreactor. Due to the low concentration of the air inside the bioreactor, the 'dispersed multiphase turbulence model' is used. This model is appropriate for a case where the concentration of the secondary phase is diluted, and the fluctuating quantities of

Table 1 – The set of equations used in this study.

Model	Mathematical Equations Equation number
Continuity equation	$\frac{\partial}{\partial t}(\rho_m \alpha_m) + \frac{\partial}{\partial x_i}(\rho_m \alpha_m u_{m,i}) = 0$ (1)
Momentum balance equation	$\frac{\partial}{\partial t}(\rho_m \alpha_m u_{m,i}) + \frac{\partial}{\partial x_j}(\rho_m \alpha_m u_{m,i} u_{m,j}) = \frac{\partial}{\partial x_j}(\alpha_m (\tau_{ij})_m) - \alpha_m \frac{\partial p}{\partial x_i} + \rho_m \alpha_m g_i + F_{Di}$ (2)
	where
	$\tau_{ij} = \mu_m (\frac{\partial u_i}{\partial x_j} + \frac{\partial u_j}{\partial x_i}) - \frac{2}{3}\delta_{ij}\frac{\partial u_i}{\partial x_i})$
Drag model	Symmetric model
	$C_D = \begin{cases} 24(1 + 0.15\,\mathrm{Re}^{0.687})/\mathrm{Re} & \mathrm{Re} \le 1000 \\ 0.44 & \mathrm{Re} > 1000 \end{cases}$ (3)
Turbulence model	**realizable k-ε**
	turbulent kinetic energy conservation equation
	$\frac{\partial(\rho k)}{\partial t} + \frac{\partial(\rho k.\, u_j)}{\partial x_j} = \frac{\partial}{\partial x_j}\left[\left(\mu + \frac{\mu_t}{\sigma_k}\right) + \frac{\partial k}{\partial x_j}\right] + G_k - \rho\varepsilon$ (4a)
	Turbulent energy dissipation rate conservation equation
	$\frac{\partial(\rho\varepsilon)}{\partial t} + \frac{\partial(\rho\varepsilon.\, u_j)}{\partial x_j} = \frac{\partial}{\partial x_j}\left[\left(\mu + \frac{\mu_t}{\sigma_\varepsilon}\right)\frac{\partial \varepsilon}{\partial x_j}\right] + \rho C_1 S\varepsilon - \rho C_2 \frac{\varepsilon^2}{k + \sqrt{\varepsilon}}$ (4b)
	where
	$C_1 = \max\left[0.43, \frac{\eta}{\eta + 5}\right], \eta = S\frac{k}{\varepsilon}, S = \sqrt{2S_{ij}S_{ij}}$ (4c)
	And turbulent viscosity for the liquid phase is calculated by
	$\mu_t = \rho C_\mu \frac{k^2}{\varepsilon} \text{and} C_\mu = \frac{1}{A_0 + A_S \frac{ku^*}{\varepsilon}}$ (4d)
	SST k-ω
	$\frac{\partial}{\partial t}(\rho k) + \frac{\partial}{\partial x_i}(\rho k u_i) = \frac{\partial}{\partial x_j}\left[(\mu + \frac{\mu_t}{\sigma_k})\frac{\partial k}{\partial x_j}\right] + G_K - Y_k$ (5a)
	$\frac{\partial}{\partial t}(\rho\omega) + \frac{\partial}{\partial x_i}(\rho\omega u_i) = \frac{\partial}{\partial x_j}\left[(\mu + \frac{\mu_t}{\sigma_\omega})\frac{\partial \omega}{\partial x_j}\right] + G_\omega - Y_\omega$ (5b)
	For G_K, G_ω, Y_k, and Y_ω refer toAnsys Fluent Theory Guide (2022).
	where the turbulent viscosity is calculated by the addition of a limiter.
	$\mu_t = \frac{\rho k}{\omega}\frac{1}{\max[\frac{1}{\alpha^+}, \frac{SF_2}{a_2\omega}]}$ (5c)
	The value of α^+, S, F_2, and a_2 are estimated (Ansys Fluent Theory Guide (2022)).
Impeller zone modeling	**Multiple Reference Frames (MRF)**
	Mass conservation
	$\frac{\partial \rho}{\partial t} + \frac{\partial(\rho u_i)}{\partial x_i} = 0$ (6a)

(continued on next page)

– Table 1 (*Continued*)

Model	Mathematical Equations Equation number
	Momentum conservation
	$\frac{\partial(\rho u_i)}{\partial t} + \frac{\partial(\rho u_i u_j)}{\partial x_j} = -\frac{\partial p}{\partial x_i} + \frac{\partial \tau_{ij}}{\partial x_j} - 2\rho\delta_{ij}\Omega_j u_k + \rho\Omega_j(\Omega_j x_i - \Omega_i x_j)$ (6b)
	Sliding Mesh (SM)
	Mass conservation for the rotational region with respect to the stationary zone
	$\frac{\partial_g}{\partial t}(\rho_m \alpha_m) + \frac{\partial}{\partial x_j}(\rho_m \alpha_m (u_{m,j} - u_g)) = 0$ (7a)
	Momentum conservation for the rotational region with respect to the stationary zone
	$\frac{\partial}{\partial t}(\rho_m \alpha_m u_{m,i}) + \frac{\partial}{\partial x_j}(\rho_m \alpha_m u_{m,i}(u_{m,j} - u_g)) = \frac{\partial}{\partial x_j}(\alpha_m \tau_{m,ij}) - \alpha_k \frac{\partial p}{\partial x_j} + \rho_m \alpha_m g_i + F_D$ (7b)

the secondary phase (air) can be given in terms of mean characteristics of the primary (liquid) phase. In this approach, the continuous phase is modeled using some version of RANS model, which is the same as a single-phase RANS model but with extra terms for the interphase momentum transfer. In the momentum equation for the dispersed phase, 'own' viscous and turbulent transport terms are ignored, while the Tchen-theory (Hinze, 1975) correlations are used for the fluid-particle interaction. The reader is referred to the ANSYS Fluent theory guide for more information on this model (Ansys Fluent Theory Guide (2022). The first model applied to the simulation is the realizable k-ε model (Eq. 4a-d), which is the most recommended model for the simulation of rotational flows among the available k-ε models. The other RANS model which is also known for its ability in modelling rotational flow is the Shear-Stress-Transport (SST) k-ω model (Eq. 5a-c,(Menter, 1994)). Both models presume the turbulent flow is (essentially or mainly) isotropic, while in fact it is not.

2.2. *Modelling the impeller rotation*

The impeller rotation is the main source of momentum inside the bioreactor. Therefore, modeling the impeller rotation is also one of the most challenging aspects of simulating a stirred bioreactor. Two main approaches have been explored and applied repeatedly in the previous decades by many researchers, such as Ng et al. (Ng et al., 1998), (Lane et al., 2000a, b), (Oshinowo et al., 2000), (Bujalski et al., 2002), (Montante et al., 2006), (Gelves et al., 2014), (Haringa et al., 2018a, b) and Cappello et al. (Cappello et al., 2021). So far, most authors have preferred – usually for large(r) stirred vessels – the Multiple Reference Frames (MRF) model over the Sliding Mesh (SM) technique because of the (much) higher computing time involved in the latter while, according to most authors, the flow fields obtained by the two methods are comparable. Li et al. (Li et al., 2018), however, reported differently for 15 mL and 250 mL bioreactors. Also, Sadino-Riquelme et al. (Sadino-Riquelme et al., 2022) reported from their simulations for a 4 L vessel that SM performed better when the dynamics of the flow field is important.

The MRF model, also known as the frozen rotor approach, is a steady-state method introduced by Luo (Luo, 1994). In the MRF model, the computational domain is divided into two zones one of which is connected to the impeller and the other one to the reactor wall. The impeller is put into a specific stationary position and the revolving motion of the liquid is mimicked by adding two terms to the Navier-Stokes equation for that zone, *viz.* a centrifugal force and a Coriolis force. These two forces mimic the effect of the revolving impeller on the fluid motions while the impeller itself is in a specific 'frozen' position (with respect to baffles or dip tubes) (Eq. 6a-b).

At the interface of the two zones, the flow is assumed to be in a steady state. The velocity vector and velocity gradients are then transformed to ensure the coupling of the two zones as well as to compute the fluxes. Therefore, the inertial frame velocity conservation is assumed across the interface, ensuring the correct velocity at the adjacent zones. The MRF model gives a fair approximation of the flow field and is reasonably accurate for a vessel with a small impeller-to-tank diameter ratio, due to the relatively weak interaction between impeller and baffles or dip tubes.

The other method is the SM approach which is a special case of a dynamic mesh model where one part of the computational domain really moves with respect to another stationary zone. In this case, a selected mesh region that includes the impeller is disconnected from the rest of the mesh in the tank and slides past the stationary tank mesh. The rotation of the moving section happens at every time step, turning this model into an essentially transient method. Then, at every time step, the data is transferred from one region to another at the interface, always coupling the two rotational and stationary regions. Due to the sliding of the rotational region with respect to the stationary region, a grid velocity (u_g) is defined which is the time rate of change at any grid point in the moving domain with the position vector. The mass and momentum conservation equations are then written for the rotational zone with respect to the stationary zone (Eq. 7a-b).

In the SM method, the re-computation of the fluxes across the two non-conformal interface zones of the interface is necessary, since, due to the grid moving against the adjacent cells, the adjacent grid faces are not necessarily aligned at the interface. Instead of the original grid interfaces, an

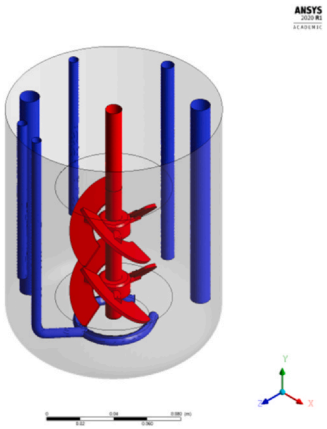

Fig. 1 – The schematic picture of the geometry of the 2 L tank in Fluent.

interpolation of the intersection of the two interface zones at each time step is being used to compute the flux at the interface. The equations used for both MRF and SM models in Fluent are presented in Table 1.

3. Simulation techniques

3.1. *Geometry and physical properties*

In the present study, a 2 L pilot plant bioreactor with a working liquid volume of 1.4 L is being simulated. The bioreactor has a diameter of $T = 0.130$ m and is filled with the liquid phase up to $H = 0.121$ m. Two pitched blade impellers with a diameter of $D = 0.05$ m agitate the fluid at a speed of $N = 250$ rpm. The bubbles are injected into the bioreactor through a ring sparger at the bottom (14 holes, d_0=0.5 mm). The vessel, shown in Fig. 1. is very similar to the bioreactor used by our industrial partner as part of a scale up process, therefore, not much experimental data is available. The impeller power number for the case of the 2-stage fully submerged impeller set with no air sparging and no inserts is N_P= 1.1, based on the catalogue provided by the vendor, corresponding to a power draw of P_u= 0.0249 W. Also, some tests have been carried out by our industrial partner to measure the gas holdup inside the bioreactor. More data about the flow characteristics inside the bioreactor is not available.

The properties of the liquid phase are ρ_l= 1003 kg/m^3 and μ_L= 0.0007 Ns/m^2. The properties of air (dispersed phase) are ρ_g= 1.225 kg/m^3 and μ_L= 1.789e-05 Ns/m^2. In this model, the Reynolds number is calculated from volume-averaged properties (density and viscosity). The air is being injected into the bioreactor at a volumetric flow rate of 14 ccm (2.33e-07 m^3/s) and the bubbles are assumed to be single-size all the way through the bioreactor with a diameter of d_B= 2.8 mm for the k-ε realizable model and d_B= 1.8 mm for the SST k-ω/k-ε model. Both SM and MRF models are being used for modelling the impeller rotation.

3.2. *Grid selection*

The current study shows that the SM method is very much dependent on the selected grid type. Different types of mesh have been used for the simulation of the bioreactor in different literature. In this study, we focus on two types of mesh, *viz.* a polyhexcore mesh and a purely polyhedral mesh. The polyhexcore mesh, also denoted as the mosaic mesh, has been introduced by ANSYS Fluent as a superior meshing technique. This technique uses a combination of different mesh types such that a high-quality layered polyprism mesh is used in the vicinity of the boundary layer while the bulk region is filled with octree hexahedral cells. The two regions are then connected using a polyhedral grid. It is claimed by Fluent that this type of grid is up to 45% faster, while it requires less than 30% RAM to provide accurate results.

On the other hand, the polyhedral mesh has been the fastest-to-converge technique of meshing before the introduction of the mosaic mesh. This type of mesh decreases the number of cells needed for the simulation compared to the tetrahedral and hexahedral grid while it accurately predicts the results using fewer computational resources.

In the current study, both mesh types have been used. Fig. 2 shows the cross-sectional view of both of them. Next to

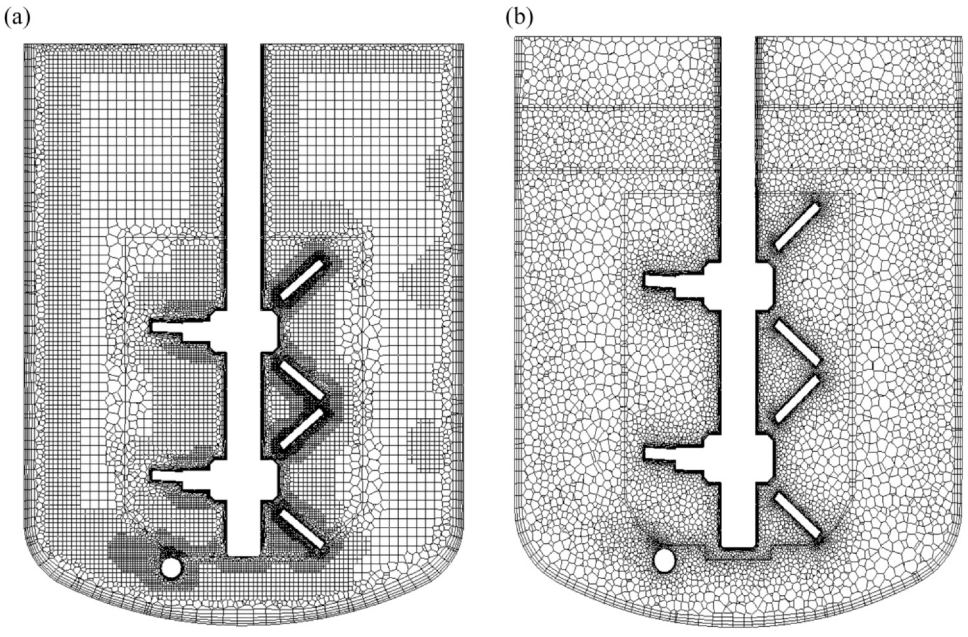

Fig. 2 – (a) the polyhexcore (mosaic) grid for the 2 L tank; (b) the polyhedral mesh for the 2 L tank.

the tank walls as well as the internal pipes, inflation layers were produced for capturing the boundary layer. The grid size is different for the polyhedral and polyhexcore meshes, and in the case of the polyhedral grid, a finer grid is used around the gas-liquid interface at the headspace. Regardless of sizing differences, the skewness has been kept smaller than 0.8 and the orthogonal quality is larger than 0.1 for both cases.

A grid independence study was also carried out for each case. For the case of the mosaic condition, 470108, 990593, and 1483,371 cells were produced, and the results showed that the simulation is independent of the grid type after 990593 cells for the mosaic mesh. The same process was also carried out for the polyhedral as well, and a similar pattern was observed. Therefore, the difference between the mosaic and polyhedral grids used in this simulation is in the spatial grid resolution, especially at the interfaces, rather than in the number of grid cells. For both mesh types selected here, the y^+ values were within the recommended range. In the mosaic grid, the y^+ on the impeller wall has a value of 12.41 which is acceptable for the realizable k-ε model with a scalable wall function. The y^+ calculated to be 12.7 and 5.41 for the realizable k-ε (with scalable wall function) and SST k-ω model, respectively, using a polyhedral mesh. Both these values were discussed with the FLUENT help centre and had been judged to be adequate for carrying out the simulation.

The time step in each simulation is calculated on the basis of tip velocity, the Courant number of 0.1, and the average cell size used for each grid type, giving a value of 0.3 ms (≈0.45 degree of an impeller revolution) and 0.2 ms (≈0.3 degree of an impeller revolution) for the mosaic and polyhedral grids, respectively.

3.3. *Interaction of the impeller zone with the internals*

The turbulence intensity is high close to the sparger where the air bubbles are being injected, as well as close to the impellers. Therefore, the interface of rotating and stationary zones should preferably be set at a distance from the high turbulence intensity regions. However, in the current case of study, the 2 L bioreactor is a complex system. It comprises five internal probes, which can act as vortex-breaking tools like baffles, as well as a ring sparger which is placed close to the impeller; they are all packed at a very small distance to the impeller and tank walls. This results in great difficulty in choosing the interface between the rotational and stationary regions. Due to this reason, the interface zone at the bottom, close to the sparger, is of a rather irregular shape; this complicates the mutual tuning of the flow fields computed in the two zones. The grid sizing needs to be more controlled in this region especially for the interface closer to the sparger. As a result, different face sizes have been chosen for this interface which ends up in a non-conformal mesh.

3.4. *Boundary conditions*

Solving the governing equations in the CFD needs the correct boundary conditions. In our study, the bubbles are injected through a ring sparger (14 holes, d_o=0.5 mm) at the bottom of the bioreactor. To prevent the high computational costs enforced by the necessity of using a finer grid close to the sparger holes, the sparger orifices are modeled through a continuous surface acting as a velocity inlet where the air is injected inside the bioreactor at a constant flow rate. All walls are no-slip walls, while the shaft wall is rotating at an absolute velocity equal to the impeller velocity. For modeling the tank's top surface, there are two methods available. The first method which has been used in several studies in the past decade is using a degassing boundary condition. In this method, only the liquid volume is being modeled and the top surface is assumed to be an exit for the gas phase, and functions as a wall for the liquid phase.

(Günyol, 2017) recommended a degassing boundary condition over a pressure outlet for cases where the impeller is close to the free surface and the gas loading is as high as 20%. Also, (Haringa, 2017) used the pressure outlet for the two-phase flow simulation of a stirred bioreactor and changed it to degassing boundary condition after the convergence was achieved. He reported steeper concentration profiles for a degassing outlet boundary condition. As we see later on, in our case study, although the top impeller is close to the free surface, the air volume fraction is less than 0.04%. One of the non-physical problems of the degassing boundary condition is that the liquid displacement after the start of the bubbling process is not considered.

Our hypothesis, however, is different from Günyol's recommendation: the use of the pressure outlet may be a better choice for cases where the impeller is close to the surface. At high velocities, an impeller close to the surface could create a vortex around the impeller shaft entrapping air from the top surface. This effect is also ignored when a degassing boundary condition is being used. Due to these reasons, the assumption of a degassing boundary condition at the top surface of the liquid does not seem to be the best approach in our case study. To investigate further the influence of the outlet boundary condition on the flow field, both degassing and pressure outlet boundary conditions are used for modeling the bioreactor in the absence and presence of the air head space, respectively.

4. Results

4.1. *Influence of outlet boundary condition*

In the current study, a degassing boundary condition (BC) is being used initially to model the outlet using the MRF method for modeling the impeller rotation. Due to the reasons mentioned in Section 3.4, another simulation is being carried out considering an air headspace at the top with a pressure outlet as the boundary condition. The mosaic grid is used for both simulations with a maximum cell size of 5 mm. The turbulence is accounted for by the realizable k-ε model.

The velocity vector plots for the two cases are shown in Fig. 3. While, at a first glance, the flow fields look rather similar for the two cases, a closer inspection may reveal that with the pressure outlet BC, the upward flow along the reactor wall is stronger and that both downward and azimuthal velocities in the central part of the reactor are higher. The two azimuthal velocity plots for the degassing BC exhibit, in red, singular high velocities (0.97 m/s) in the near vicinity of the impeller blades. With the pressure outlet BC, such high velocities do not occur to the same extent: they are found at different positions and the maximum velocity is just 0.74 m/s. These high velocities, in excess of the impeller tip speed (0.65 m/s), are claimed to be spurious (numerical artifacts). More details on these spurious velocities are presented in chapter 5.

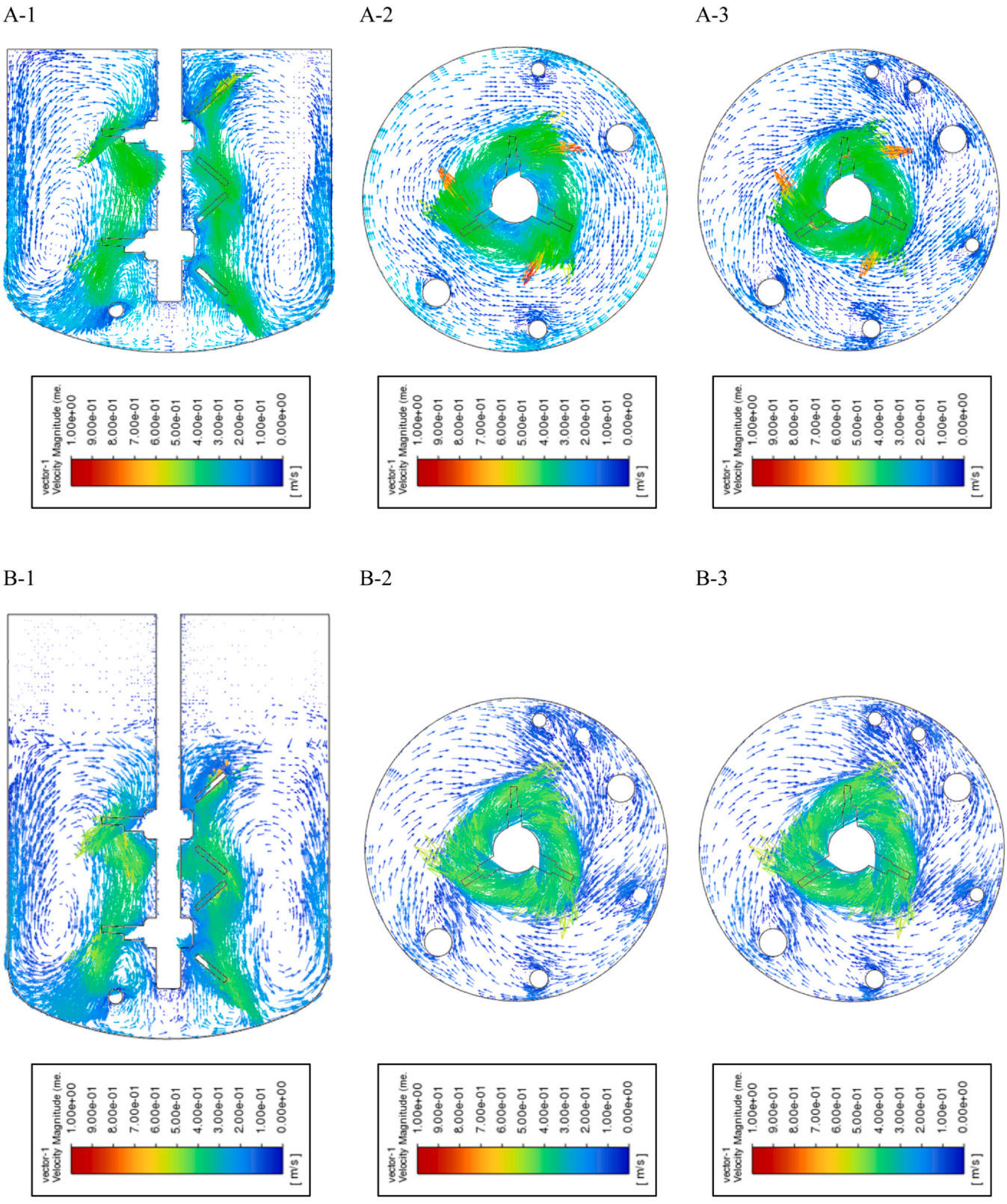

Fig. 3 – The velocity vector plot for the MRF method and the mosaic grid for (A) the degassing boundary condition and (B) a pressure outlet boundary condition at (1) a vertical plane, (2) the horizontal cross-section around the bottom impeller, and (3) the horizontal cross-section around the top impeller.

The air volume fraction contours for the two cases are plotted in Fig. 4. Note air volume fractions are low overall, the maximum value being just 0.03%. When using the pressure outlet BC, the air volume fraction seems to be very low or nihil in the rotor section, as it looks as if all bubbles injected bypass, or do not enter, the impeller zone. This might be due to the use of the MRF technique in which the impeller is at a fixed stationary position.

With the pressure outlet BC, a small dip in the liquid level is captured around the shaft which is not found with the degassing BC. With degassing BC, keeping the liquid surface flat, the liquid phase is forced to turn downwards such that some of the

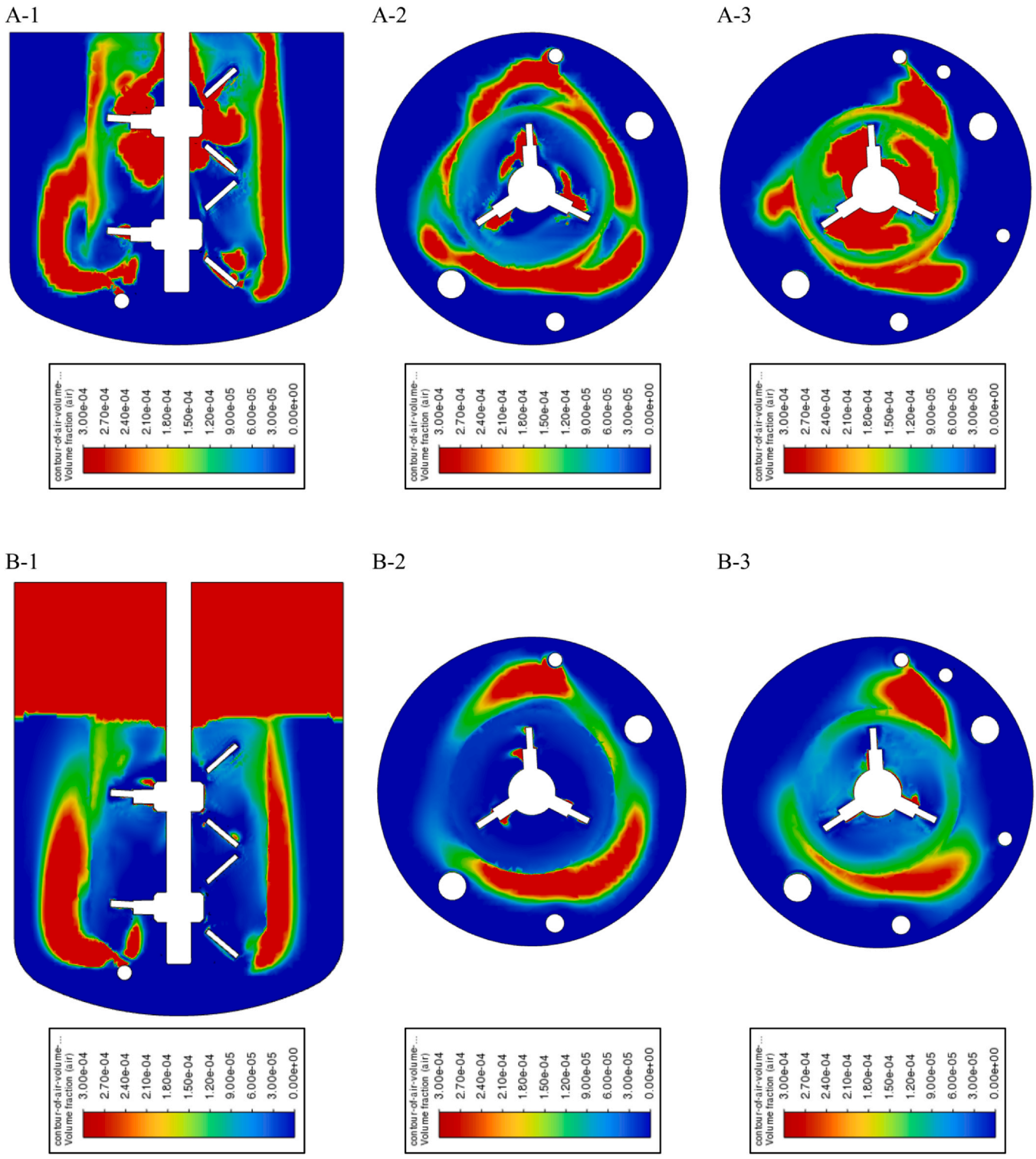

Fig. 4 – The air volume fraction contour for the MRF method and the mosaic grid for (A) the degassing boundary condition and (B) the pressure outlet boundary condition at (1) a vertical plane, (2) the horizontal cross-section around the bottom impeller, and (2) the horizontal cross-section around the top impeller.

bubbles might get entrapped in this downflow. This downflow increases the air volume fraction first of all around the top impeller but to a lesser degree also at the lower impeller. This is largely in line with reports by Günyol and Haringa in their PhD theses (Günyol, 2017; Haringa, 2017).

The tentative overall conclusion is that ignoring the headspace above the liquid and the pertinent use of the degassing BC is rather unfortunate, at least for simulating this 2 L bioreactor, as it forces the liquid surface to remain flat despite the close proximity of the impeller. The formation of a vortex, creating a dip in the liquid surface around the impeller axis, is deliberately ignored. The second objection relates to a mass balance issue when aeration is started in a liquid-full domain. For these reasons, the degassing BC for a liquid-full domain will be abandoned in the remainder of this paper. Given that the gas phase seems to bypass the impeller zone, the next section is about assessing the difference between the MRF and SM techniques.

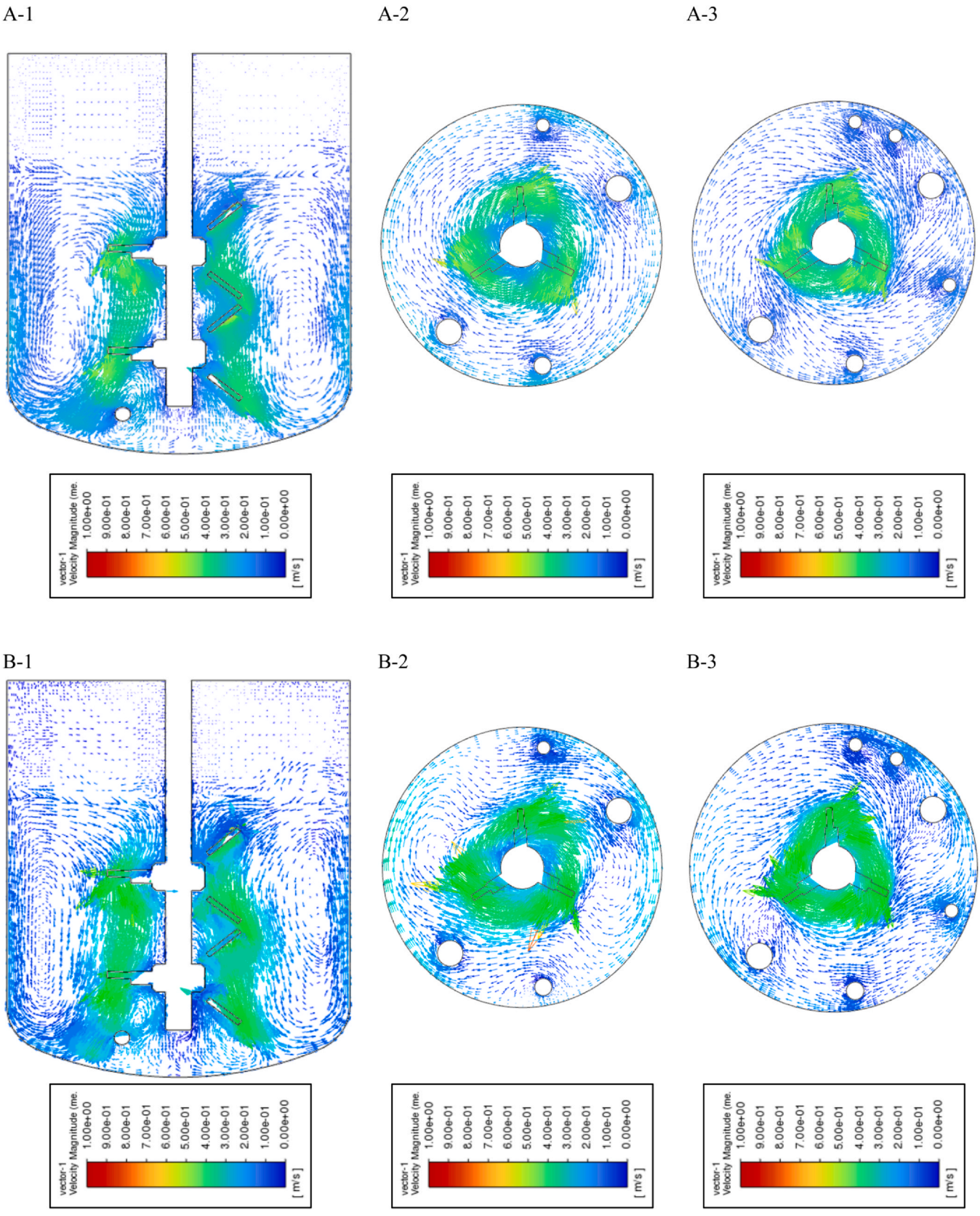

Fig. 5 – The velocity vector plot using the mosaic grid, the realizable k-ε model and d_B= 2.8 mm for (A) MRF method (B) SM method at (1) a vertical plane, (2) the horizontal cross-section around the bottom impeller, and (2) the horizontal cross-section around the top impeller.

4.2. *MRF vs. SM for modeling the impeller motion*

The SM flow fields, and air volume fraction results presented in this Section have been obtained by switching MRF simulations into SM. This implies that in both cases the same mosaic grid and the same realizable k-ε turbulence model were used, as in the previous Section 4.1.

The flow field results for both the MRF and SM cases are presented in Fig. 5. Note that the MRF case is about a steady-state simulation, while the SM is just a snapshot from a

Table 2 – Comparison of the flow properties from the numerical simulations with the experimental values for the effect of the impeller modelling technique.

		$\dot{m}_{air,inlet}$	$\dot{m}_{air,outlet}$	U_{tip}	$\alpha_{g,exp}$
Experimental		2.85e-07		0.65	0.0067
		$\dot{m}_{air,inlet}$	$\dot{m}_{air,outlet}$	U_{max}	α_g
Numerical	MRF	2.85e-07	2.82e-07	0.79	0.0053
	SM	2.85e-07	2.84e-07	0.85	0.0123

transient simulation, taken at 12 s of real time which is similar to impeller position in MRF simulation. Fig. 5 shows that both cases predict rather similar velocity fields, except that panel B2 of Fig. 5 exhibits some vortical motions. In addition, the SM flow field suffers from spurious velocities to a higher degree than the MRF flow field, *viz.* 0.85 m/s *vs.* 0.79 m/s, both being higher than the impeller tip speed (0.65 m/s). This will again be discussed in greater detail in chapter 5. Regardless of the velocity field, the SM case gives a slightly better result for the air mass flow rate conservation (Table 2).

The air volume fraction results are plotted in Fig. 6 and despite very similar results for the liquid velocity field, the SM acts very differently from the MRF. In the steady-state MRF case, the gas phase hardly enters the impeller zone as it may be kept trapped inside the steady elongated vertical flow structure, while the dynamic nature of the SM flow field may be able to disperse the gas phase much better. As soon as the simulation was changed to SM, however, the volume average of the air volume fraction starts to increase inside the bioreactor, particularly around the upper impeller. Yet, a discontinuity is still observed at the interface of the rotational and stationary zones. This issue could be considered a result of the insufficient grid resolution at the interface, which suggests the SM mesh simulation may be very sensitive to mesh type and quality, not only in predicting the liquid velocity field but also in reproducing the air volume fraction inside the bioreactor.

4.3. *Influence of the mesh type selection*

Running the above simulations on meshes of varying resolution suggested that particularly the SM type of simulation is highly dependent on the quality of the mesh. In addition, the main reason why spurious velocities show up may be in the grid quality and in local mismatches between the grid and flow field. Therefore, a sensitivity study is carried out to study the influence of the grid type selection by using a polyhedral grid in addition to the Fluent recommended mosaic type of grid. Several mesh resolutions are tested, and the results show that a mesh that works for the MRF case study will not necessarily work when the SM method is set for the rest of the simulation. The new results with the polyhedral grid displayed in this section are for the SM simulation only and are compared with SM results obtained with the mosaic grid from the previous section.

The velocity vector plots for the mosaic and polyhedral cases are presented in Fig. 7. The vectors plotted in the vertical cross-sections show that with the polyhedral grid, velocities are slightly larger than those obtained on the mosaic grid. In the horizontal cross-sections around the bottom and top impellers, singular large (red) velocity vectors are again seen on the blade surfaces, though at different positions for the mosaic and polyhedral grids: see chapter 5. These allegedly spurious vectors are larger for the bottom impeller. The maximum velocity predicted on the mosaic grid is 0.85 m/s while the polyhedral grid produces a maximum velocity equal to 1.11 m/s (Table 3) which is almost two times bigger than the tip speed.

The contours for the air volume fraction are plotted for both grid types in SM simulations in Fig. 8. Comparing the air volume fraction contours for the two cases shows that although the polyhedral grid is not optimal for reproducing the liquid velocity field, it performs well in predicting the air volume fraction. The air volume fraction especially in the rotational zone is significantly higher on the polyhedral grid, while also the spatial distribution is better. As remarked before, in the case of the mosaic grid, the air largely bypasses the rotational zone. The position of the impeller was deliberately taken different between the two cases, to illustrate the effect of the interaction between impeller and dip tubes.

A comparison of the air mass flow rate conservation, however, shows that with the polyhedral grid mass conservation is less accurate than with the mosaic grid (Table 3). On the contrary, the volume-averaged air volume fraction and our experimental gas holdup agree far better with the polyhedral grid than with the mosaic grid.

4.4. *The influence of the turbulence model and bubble size*

In the last part of our study, the influence of the turbulence model combined with the bubble size is looked into for an SM simulation. Up to this point, all simulations were carried out using the realizable k-ε model with a 2.8 mm bubble size. At this point, the turbulence model was shifted to SST k-ω. The SST k-ω model has been suggested for cases where the flow is rotational, and pressure gradients are high, similar to the lab-scale bioreactor used in this simulation. Also, in an attempt to decrease the instabilities that was observed during the previous simulation, especially for the maximum velocity values, the bubble size was decreased to a smaller value of 1.8 mm. The velocity vector plots for these two cases calculated with the help of a polyhedral mesh are presented in Fig. 9.

The flow field in the vertical plane shows higher velocities in the case of the SST k-ω model with a 1.8 mm bubble size compared to realizable k-ε with a 2.8 mm bubble size. In the horizontal cross-sections around the two impellers, however, SST k-ω predicts smaller velocities in the immediate vicinity of the impellers than realizable k-ε, while the velocity magnitudes further away from the impeller are rather similar. About what we conceive as spurious velocities: with the realizable k-ε model, they originate at the locations where the blades are connected to the shaft, while smaller spurious velocities are found at the blade tips; on the contrary, with SST k-ω, the largest spurious velocities at the bottom impeller are observed just at the blade tips. More data on these maximum velocities are presented in chapter 5.

The air volume fraction contours for the two cases (Fig. 10) do not show much difference around the impeller in the vertical cross-section, except that closer to the wall and near the liquid surface at the top, the SST k-ω model predicts slightly higher air volume fractions than the realizable k-ε model. The air volume fractions in the horizontal cross sections around the two impellers also look similar, except for a small area between the blades of the top impeller where with SST k-ω smaller air volume fractions are found than with

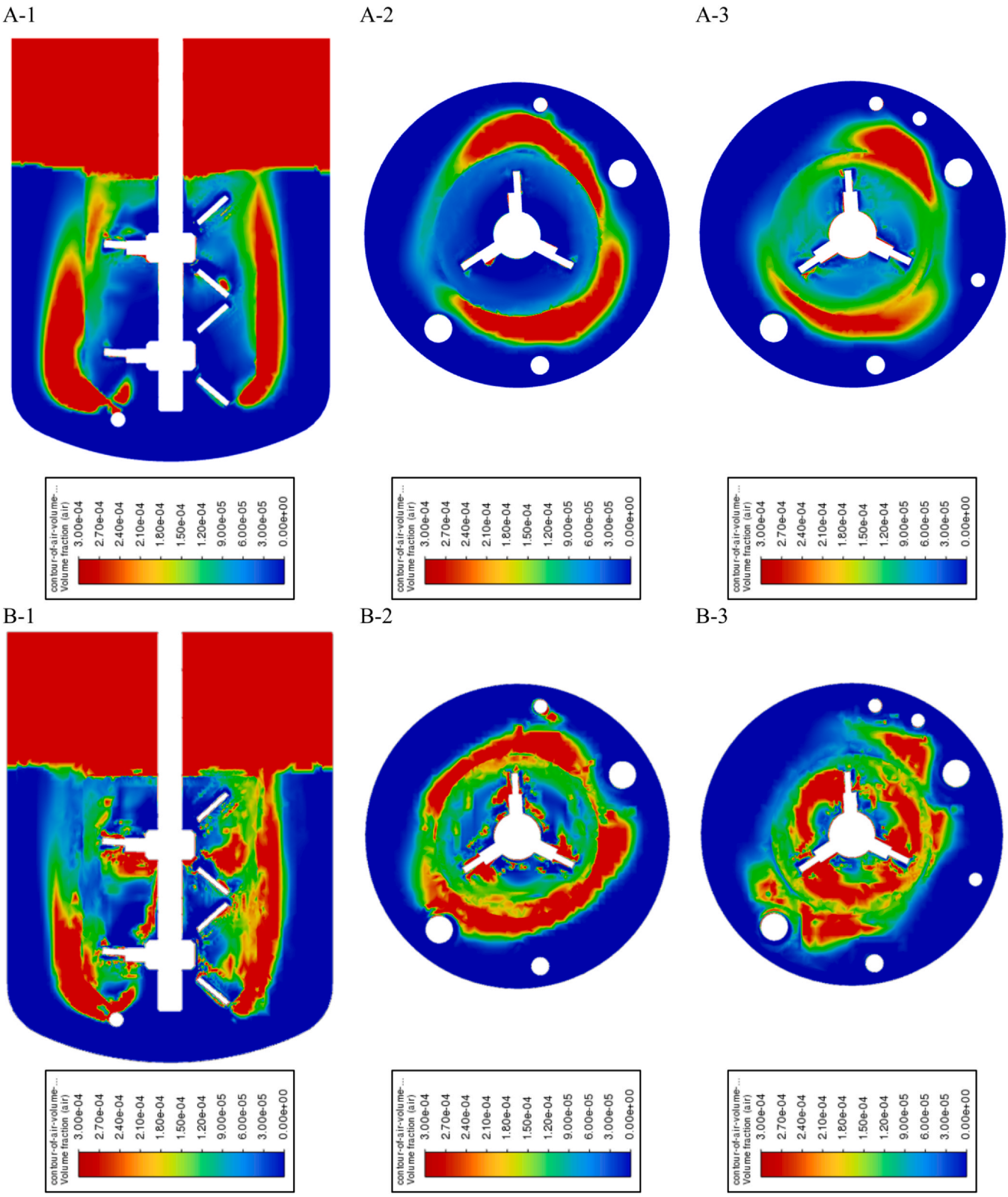

Fig. 6 – The air volume fraction contour using the mosaic grid, the realizable k-ε model and d_B= 2.8 mm for (A) MRF method (B) SM method at (1) a vertical plane, (2) the horizontal cross-section around the bottom impeller, and (2) the horizontal cross-section around the top impeller.

realizable k-ε. Since the influence of both the turbulence model and bubble size is studied together, it is not obvious if these small differences are happening as a result of the turbulence model or are due to different bubble sizes. A comparison of the air mass conservation rate for the two cases (Table 4) shows that SST k-ω with d_B= 1.8 mm model performs much better than realizable k-ε with d_B= 2.8 mm. Similar to the previous section, to illustrate the effect of the interaction between impeller and dip tubes, the position of the impeller was deliberately taken different for the two cases.

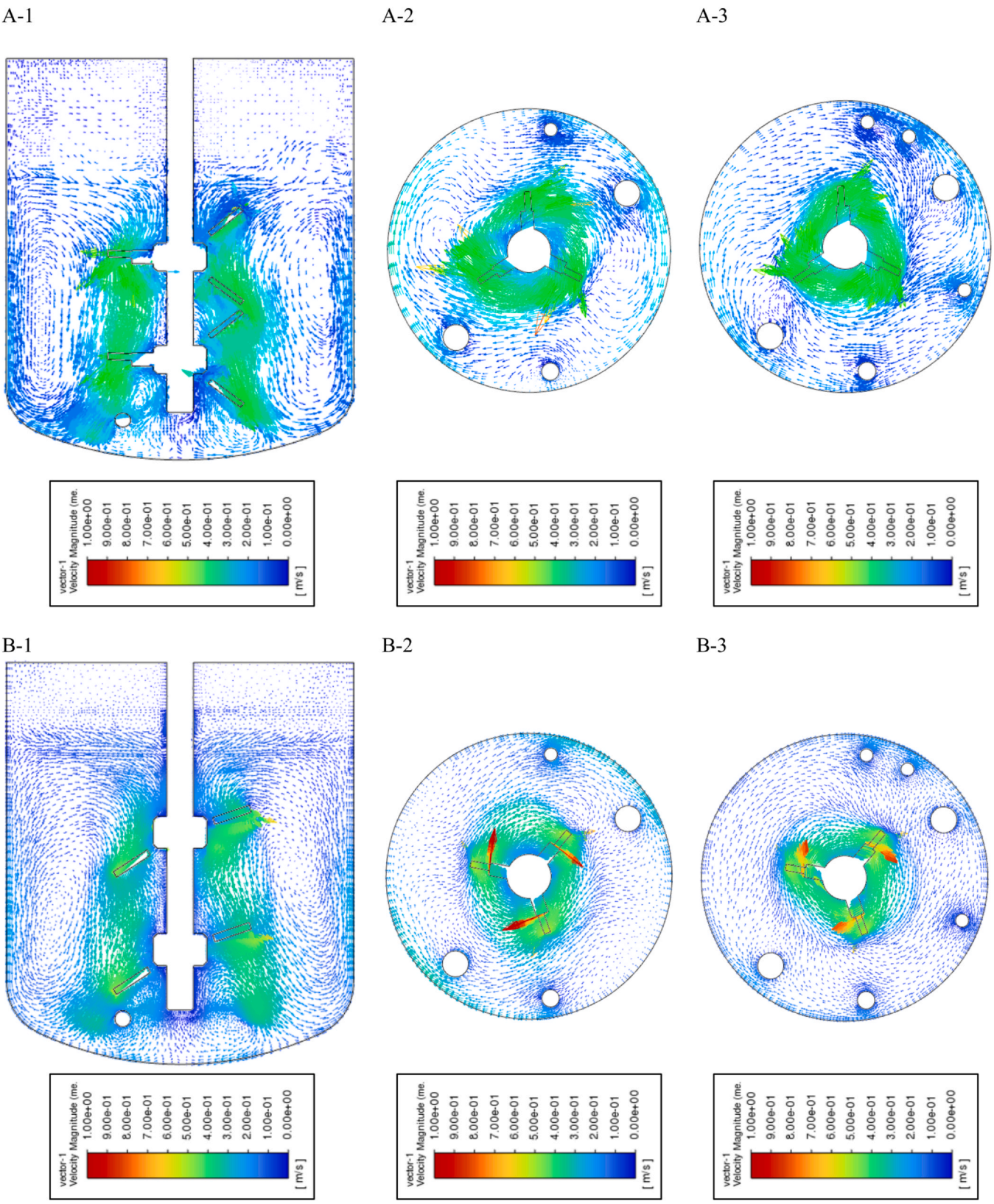

Fig. 7 – The velocity vector plot using the SM model and the realizable k-ε, d_B= 2.8 mm, for (A) mosaic grid type (t = 12 s) and (B) polyhedral grid type (t = 11 s), at (1) a vertical plane, (2) the horizontal cross-section around the bottom impeller, and (2) the horizontal cross-section around the top impeller.

5. Discussion

Our study is primarily a sensitivity study into the effects of boundary condition at the liquid surface, impeller treatment, mesh type, turbulence model, and imposed bubble size on fluid flow field and air volume fraction. We did not exhaustively explore all possible combinations of these alternative options, and we also did neither include all available k-ε models nor all alternative drag force expressions and other phase interaction forces such as lift forces. Such comprehensive studies can be found in the TU Delft PhD theses of Günyol and Haringa with large-scale fermenters in

Table 3 – Comparison of the flow properties from the numerical simulations with the experimental values for the influence of the grid type selection.

		$\dot{m}_{air,inlet}$	$\dot{m}_{air,outlet}$	U_{tip}	$\alpha_{g,exp}$
Experimental		2.85e-07		0.65	0.0067
		$\dot{m}_{air,inlet}$	$\dot{m}_{air,outlet}$	U_{max}	α_g
Numerical	Mosaic grid + SM	2.85e-07	2.84e-07	0.854	0.0123
	Polyhedral grid + SM	2.85e-07	2.75e-07	1.11	0.0084

mind. Instead, our study focused on aerated lab-scale bioreactors and took a stepwise approach guided by the lessons learnt from the theses by Günyol and Haringa and many other sources in the open literature.

We have hardly any experimental data available for validating our simulation results. The impeller used has a power input of 0.025 W and the reported air volume fraction is as low as 0.0067. The latter value is so low that one may wonder whether a two-fluid approach is meaningful anyhow. Yet, our simulations proceeded successfully and produced meaningful data. which look meaningful given the wealth of experimental and computational data reported in the open literature. Of course, the lack of experimental data for a more rigorous validation of our computational results is due to the limited availability of experimental facilities and signals the increased confidence in the CFD technique as a substitute for experimental data from a lab. This paper is intended as a more rigorous assessment by comparing various CFD options.

In the past, the use of the SM method was generally avoided due to the high computational costs compared to MRF simulations. However, the technology is on our side since the computational resources have progressed incredibly compared to one decade ago. Fluent's capability to parallel processing was used for running SM simulations on high-performance computational resources. Yet, the simulation of the SM cases could take any time between 1 week to 1 month, depending on grid resolution, time step, and the number of computational cores used, while the simulation of an MRF case was fast-paced and took at most 2–3 days. Regardless of the simulation time, we conclude that MRF is not the most accurate method in the case of modeling a lab-scale stirred bioreactor with inserts. This was also reported by (Gentric et al., 2005) for industrial-scale multi-phase chemical reactors, by (Lane, 2015) and (Li et al., 2018) although other authors (Deglon and Meyer, 2006; Koh and Schwarz, 2006; Koh et al., 2003) reported MRF simulations to be adequate. At least for small-scale stirred tanks with strongly dynamic flow features, we strongly suggest running SM simulations on high-performance computational machines to arrive at more reliable and transient flow fields.

5.1. *Mesh effects*

The frequent occurrence of singular large velocity vectors (larger than the impeller tip speed of 0.65 m/s) in the vicinity of the impellers prompted a more comprehensive study of the meshing aspect of the simulations. The shape and the position of the interface between inner (impeller) and outer (stationary) zones was one of the most challenging aspects of the simulation. Due to the small size of the tank and the presence of several internal probes as well as the short distance between sparger and impeller, it was not possible to choose a regular cylinder for the shape of the rotating zone. Instead, the interface close to the sparger was broken stepwise into smaller pieces. One may wonder whether by doing these all-basic assumptions of the MRF and SM techniques are satisfied, *e.g.*, that the velocities normal to the interface match. This practice of strongly varying and adapting the shape of the interface between the two zones frequently caused convergence issues, particularly in the case of the SM based simulations.

In our study, also the use of various mesh types was explored, among which is the tetrahedral grid. While the MRF simulation using this grid proceeded smoothly and produced a good result for the mass conservation of the air, the SM simulation on this grid was facing many difficulties and produced illogical results for both velocity and air volume fraction. This pushed us toward using mesh types such as polyhedral and mosaic. Even with the polyhedral and mosaic grids, however, despite their successful implementation in combination with the MRF method, the simulation again suffered from convergence issues upon shifting from MRF to SM. This was especially the case with the mosaic grid. These experiences show that a grid type that works for an MRF based simulation, not necessarily is a good choice for an SM case.

A rigorous assessment of grid size as generally recommended (by doubling the number of grid cells in each direction) was hardly doable: our grids were unstructured, needed grid refinement at the interface between impeller zone and stationary zone, and had to accommodate a number of inserts as well as the aeration ring. Typically, we were able to globally increase the number of grid cells in each direction by some 40% without noticing much change in the flow field.

During our simulations, we did continuously check two important aspects of the meshing: first, that at the many walls in our domain the y^+ values were in the recommended range for impeller and tank's walls for each turbulence model, and second, that the ratio of grid cell sizes to estimated Kolmogorov length scales had a proper value. While in the bulk of the flow both grid cell size and Kolmogorov length scale vary across the flow domain, typical grid cell sizes were in the range 0.8 – 1.3 mm, while Kolmogorov length scales typically were between 0.04 and 0.07 mm, resulting in ratios in the range 15–20 which seems reasonable for a RANS based simulation. Such ratios are rather similar to those reported by (Lane, 2015) although in his impeller zone the ratio may have been as low as 10.

Note that in all our simulations grid cell sizes were smaller than the imposed bubble size (1.8 and 2.8 mm). This disagrees with the Milelli-criterion that says grid cell size should be bigger than bubble size. However, in a two-fluid simulation, the two phases are continua and the grid does not see individual bubbles (Van den Akker, 2015). Bubble size is only used for calculating fluid-particle interaction forces. In addition, our volume fractions are very low.

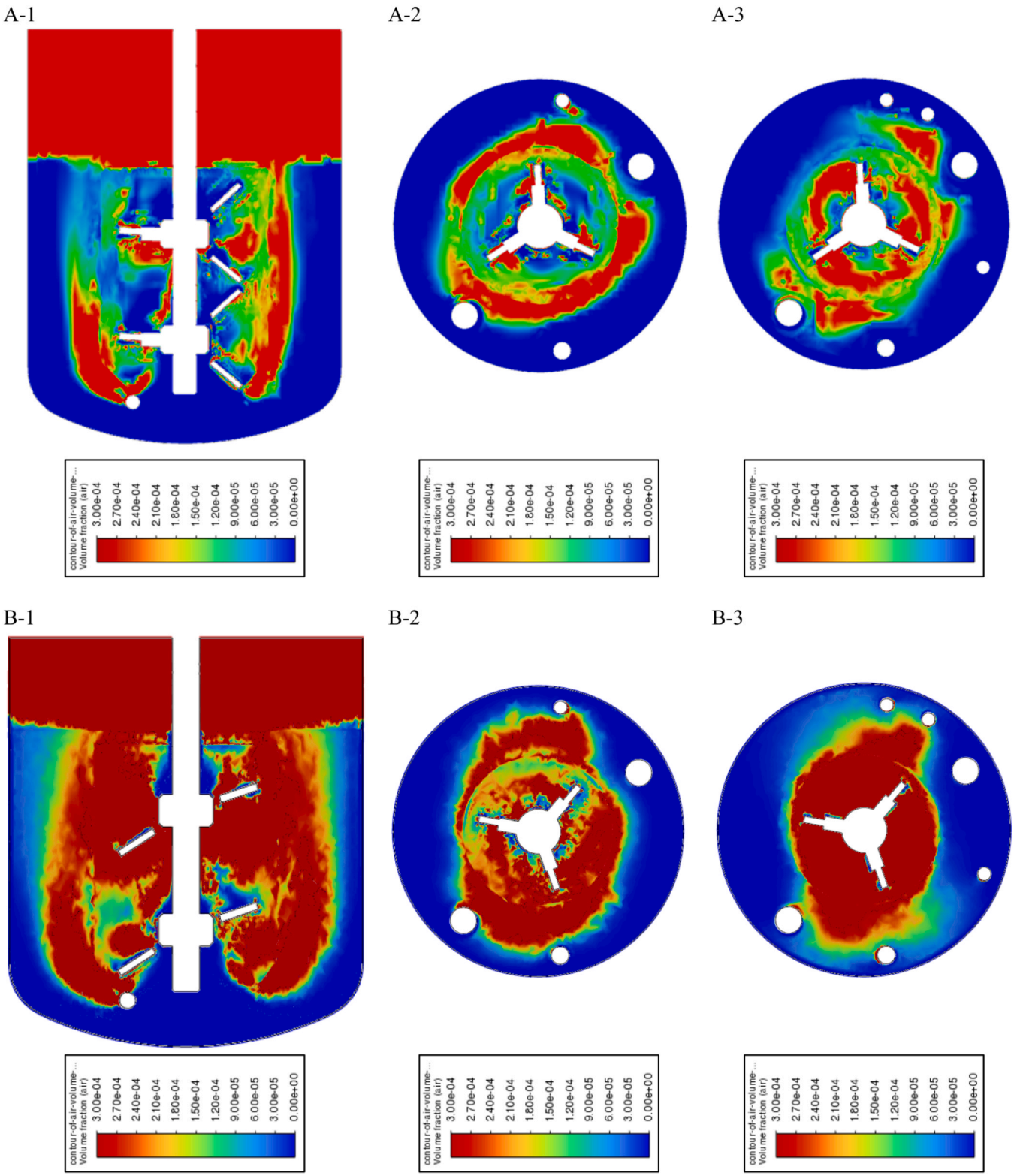

Fig. 8 – The air volume fraction contour using the SM model, the realizable k-ε model and d_B= 2.8 mm, for (A) mosaic grid type (t = 12 s) and (B) polyhedral grid type (t = 11 s) at (1) a vertical plane, (2) the horizontal cross-section around the bottom impeller, and (2) the horizontal cross-section around the top impeller.

5.2. *Power draw*

In Table 5, simulation data for power draw are reported. In all our simulations, the power draw obtained from the torque experienced by the impeller are of the order 0.1 W, *i.e.*, much higher than the 0.025 W for the unaerated vessel without internals. At the same time, the power draw found by integrating the spatial ε-distribution decreased (in the order of the simulations performed) from 0.051 W to 0.016 W. All these values are lower than the power draw found *via* the torque. In the k-ε cases, the power dissipated in the liquid bulk is some 50% of the torque-based power draw only. This is in line with the finding by (Yeoh et al., 2004) who reported their RANS model under-predicted the overall ε by 45%. These discrepancies illustrate the widely known observation (Coroneo et al., 2011; Hartmann et al., 2004; Montante et al.,

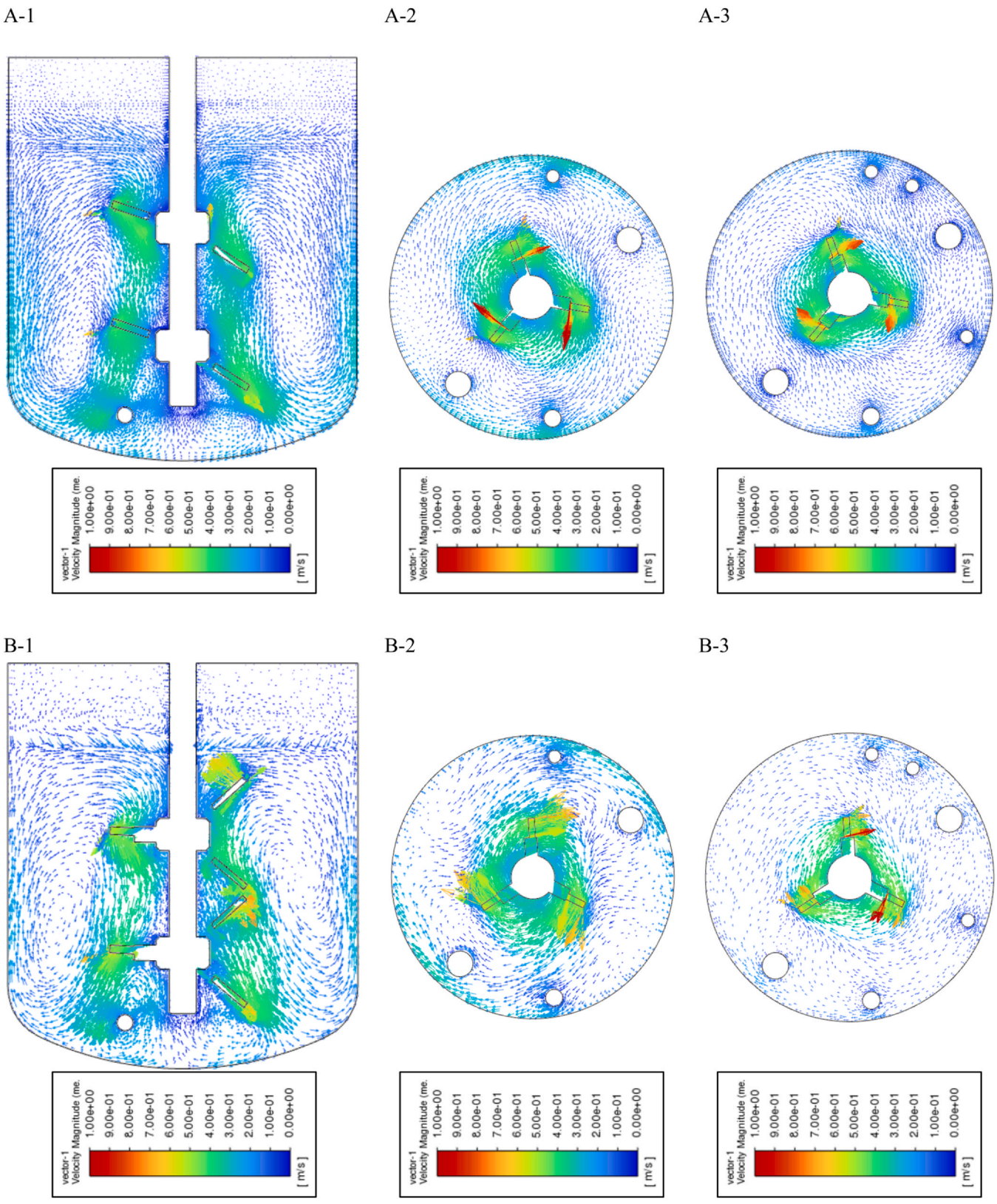

Fig. 9 – The velocity vector plot for the polyhedral grid using the SM method with (A) a realizable k-ε model and d_B= 2.8 mm; (at close to t = 12 s, same case as Fig. 8B) and with (B) the SST k-ω model and d_B= 1.8 mm (t = 12 s), in (1) a vertical plane, (2) a horizontal cross-section around the bottom impeller, and (2) a horizontal cross-section around the top impeller.

2001; Van den Akker, 2006)] that all RANS-based simulations typically under-predict turbulence levels and energy dissipation rates.

Like all RANS-based models, k-ε and k-ω turbulence models presume the turbulent flow to be essentially isotropic, thereby allowing for the hypothesis of a single turbulent viscosity. In addition, these k-ε and k-ω turbulence models may suffer from approximations and inconsistencies in the phenomenological transport equations for k, ε and ω. In the simulations of current interest, the close proximity of impeller, aeration device, baffle and dip tubes and their interactions with the flow field may turn the turbulent flow

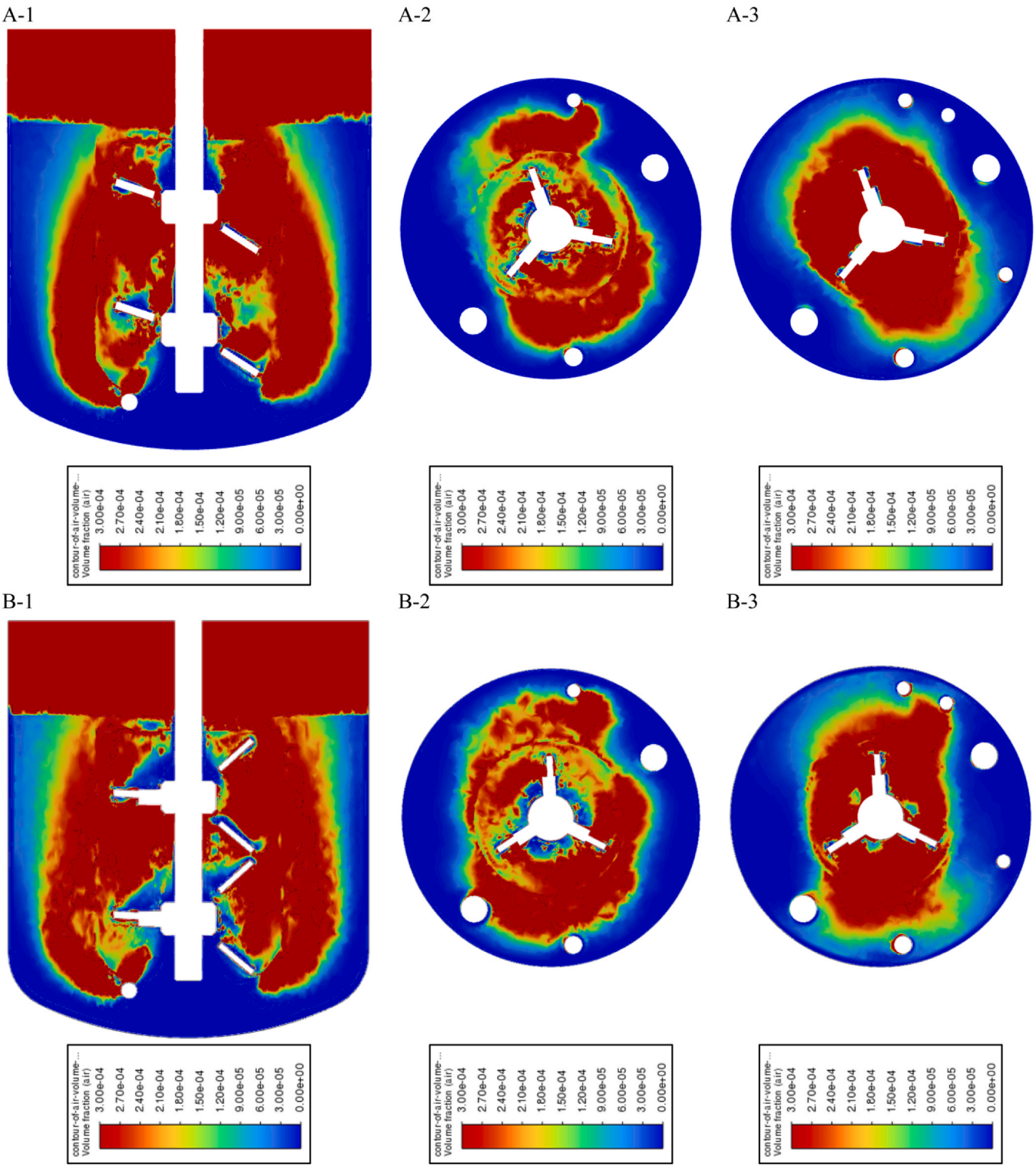

Fig. 10 – The air volume fraction contour for the polyhedral grid using the SM method with (A) a realizable k-ε and d_B= 2.8 mm (at close to t = 12 s, same case as Fig. 8B) and (B) the SST k-ω and d_B= 1.8 mm (t = 12 s) at (1) a vertical plane, (2) the horizontal cross-section around the bottom impeller, and (2) the horizontal cross-section around the top impeller.

Table 4 – Comparison of the flow properties from the numerical simulations (SM, polyhedral mesh) with the experimental values for the influence of the turbulence model and bubble size.

		$\dot{m}_{air,inlet}$	$\dot{m}_{air,outlet}$	U_{tip}	$\alpha_{g,exp}$
Experimental		2.85e-07		0.65	0.0067
		$\dot{m}_{air,\ inlet}$	$\dot{m}_{air,outlet}$	U_{max}	α_g
Numerical	Realizable $k-\varepsilon$, d_B= 2.8 mm	2.85e-07	2.75e-07	1.11	0.0084
	SST $k-\omega$, d_B= 1.8 mm	2.85e-07	2.85e-07	1.037	0.0068

Table 5 – Comparison of the experimental power with power calculated based on torque (P_T) and based on energy dissipation (P_ε) from the simulation.

					P_u (W)	
Experimental	No aeration and no internal probe exist during the input power measurements.				0.0205	
	Impeller model	Mesh type	Turbulence model	d_B (mm)	P_T(W)	P_ε (W)
Numerical	MRF	Mosaic	Realizable $k-\varepsilon$	2.8	0.093	0.051
	SM	Mosaic	Realizable $k-\varepsilon$	2.8	0.114	0.0358
	SM	Polyhedral	Realizable $k-\varepsilon$	2.8	0.104	0.0365
	SM	Polyhedral	SST $k-\omega$	1.8	0.096	0.016

very anisotropic with interacting wakes behind all inserts. And although the air volume fractions are very low, turbulence levels may be affected by the air bubbles. After all, one may even wonder (Schubert, 1986) whether in our small vessel with several inserts the turbulent flow is sufficiently well developed such that all our turbulence models and

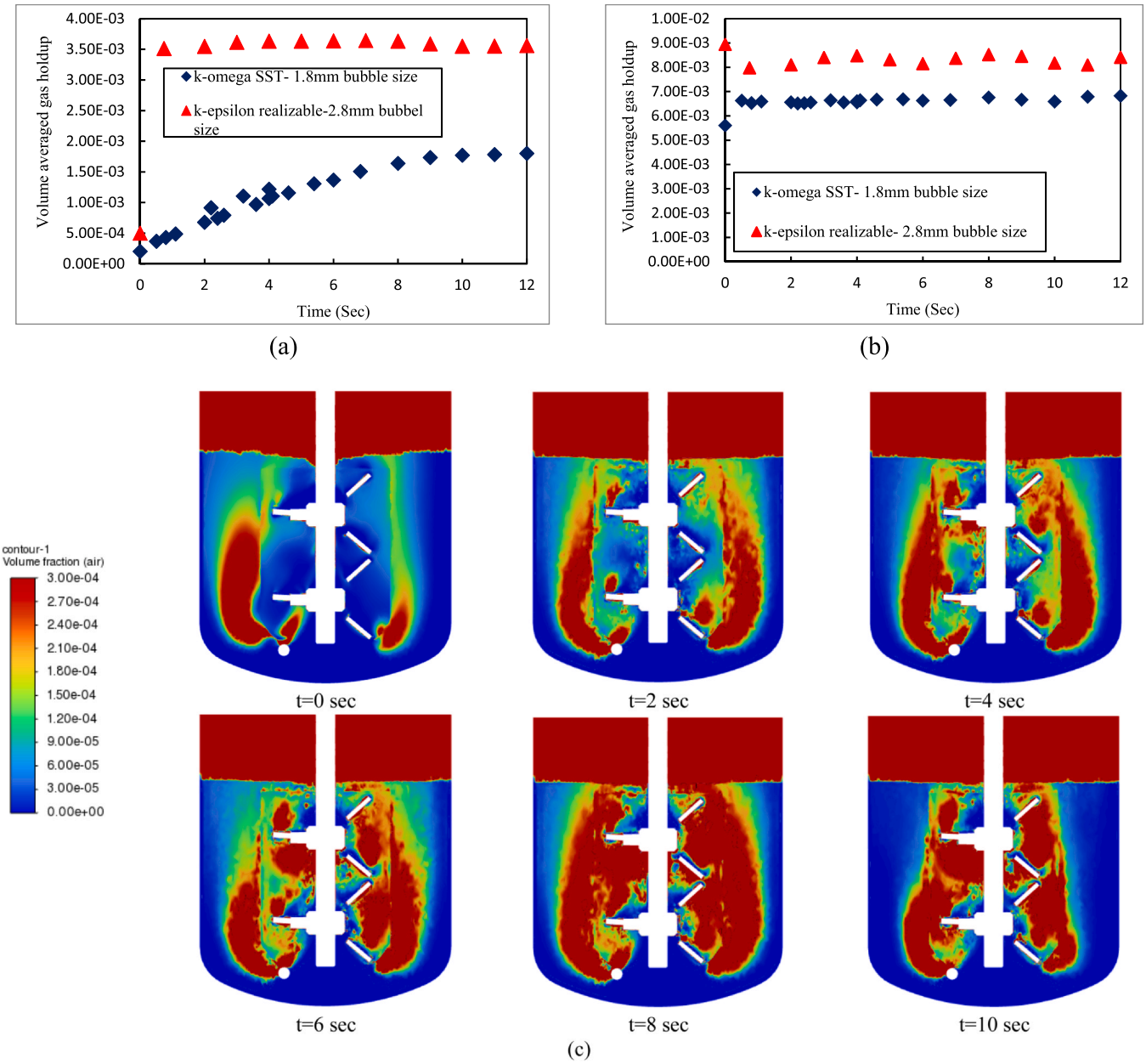

Fig. 11 – Development of the air volume fraction after the moment that the converged MRF simulation had been switched to SM on the polyhedral grid: for two different turbulence models and bubble diameters for (a) the rotational zone only, (b) the overall volume, and (c) Gas holdup development inside the bioreactor shown for a vertical cross-section for SST k-ω, and d_B= 1.8 mm.

transport equations hold. As a result, our two-fluid simulations may be rather challenging, particularly with respect to energy dissipation.

An obvious question is why the SST k-ω model produces a much lower overall energy dissipation rate than the k-ε model used. It is interesting to refer here to the paper by (Lane, 2015) who investigated how a k-ε model and various SST models, along with different mesh sizes, affected the total energy dissipation rate. Lane concluded that in terms of integrated dissipation rate values, the k-ε model seems "more satisfactory", in contrast with the finding that SST performs better with respect to flow pattern and the spatial distribution of turbulence. The latter aspect may be relevant for our lab-scale reactor where the inserts may ask for an improved description of wall-bounded flows and flow separation effects, although the interaction of all these insert-related flow features may be too much of a challenge. In addition, an additional difference between our k-ε and k-ω cases is in the imposed bubble size which was 2.8 mm for all k-ε cases and 1.8 mm for the k-ω case. At least this difference may need further study.

Taking refuge to Large-Eddy Simulations (LESs) may be the way to go. LESs do not need transport equations for k, ε and ω. Spatial distributions of ε have to be calculated off-line afterwards. Giacomelli and Van den Akker (Giacomelli and Van den Akker, 2020), (Kuschel et al., 2021), and (Thomas et al., 2021) reported that their M-Star simulations gave a far better agreement between experimental power draw data and simulation-based values, both torque-based and from the integrated ε-field. Note that in such LES-based approaches the second (dispersed air) phase is to be treated in a Lagrangian way by tracking huge numbers (millions) of individual bubbles.

5.3. *Air volume fraction*

The simulated air volume fractions reported in Tables 2– 4 vary rather wildly, with the eventual value 0.0068 obtained with the SST k-ω model and d_B= 1.8 mm being very close to the experimental value of 0.0067. Previously, (Kerdouss et al., 2008) also observed a rather disrupted air volume fraction contour during their simulation.

As starting a transient SM simulation from an initially stagnant state may be time-consuming, starting a steady-state MRF to switch to SM later on may look appealing with the view of saving computer time. Pursuing this approach, we observed after this switch a remarkable and gradual increase in the volume averaged air volume fraction towards an essentially higher value. This is illustrated for two cases in Fig. 11–a and Fig. 11–b for the realizable k-ε (d_B=2.8 mm) and SST k-ω model (d_B=1.8 mm), respectively, the data at t = 0 representing the value for the converged MRF case. The development of the gas holdup from t = 0 to t = 10 s in a vertical cross-section is shown in Fig. 11–c, for the SST k-ω model (d_B=1.8 mm) case only. This increase in air volume fraction was especially significant in the rotational zone.

Note that, as reported above, in all MRF simulations, the gas holdup largely bypasses the rotating region, as opposed to SM cases. Evidently, running first an MRF simulation to provide a better initial condition for an SM simulation is not a practice to be recommended.

5.4. *Spurious velocities*

In our search for the mesh that worked best for both MRF and SM based simulations, velocity vectors with a magnitude in excess of the tip speed (0.65 m/s) were continuously observed.

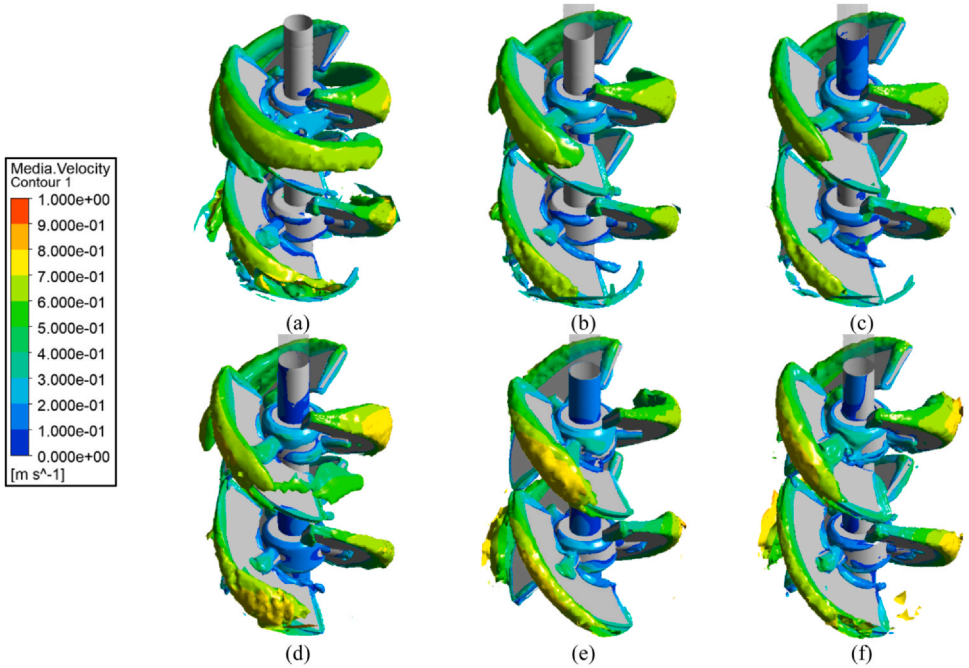

Fig. 12 – The Q =1066.3 s-2 surfaces around the impeller blades coloured by the liquid velocity magnitude for (a) the MRF impeller model with k-ε model (d_B=2.8 mm) and degassing BC in a mosaic grid, (b) the MRF impeller model with k-ε model (d_B=2.8 mm) and pressupressure outlet BC in a mosaic grid, (c) the MRF impeller model with realizable k-ε model (d_B=2.8 mm) and pressure outlet BC in a mosaic grid, (d) the SM impeller model with realizable k-ε model (d_B=2.8 mm) and pressure outlet BC in a mosaic grid, (e) the SM impeller model with realizable k-ε model (d_B=2.8 mm) and pressure outlet BC in a polyhedral grid, and (f) the SM impeller model with SST k-ω model (d_B=1.8 mm) and pressure outlet BC in a polyhedral grid.

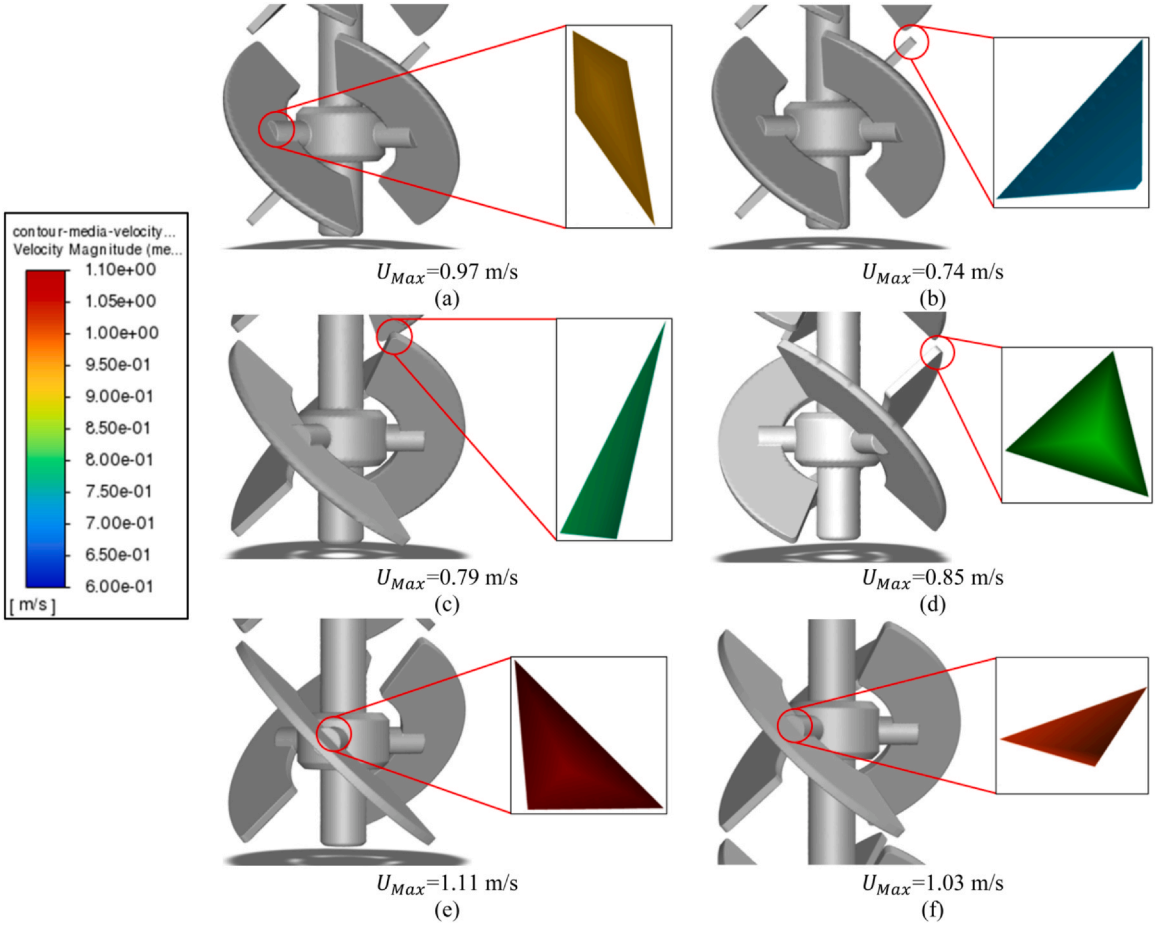

Fig. 13 – The location of the numerical maximum velocity in (a) the MRF impeller model with k-ε model (d_B=2.8 mm) and degassing BC in a mosaic grid, (b) the MRF impeller model with k-ε model (d_B=2.8 mm) and pressure outlet BC in a mosaic grid, (c) the MRF impeller model with realizable k-ε model (d_B=2.8 mm) and pressure outlet BC in a mosaic grid, (d) the SM impeller model with realizable k-ε model (d_B=2.8 mm) and pressure outlet BC in a mosaic grid, (e) the SM impeller model with realizable k-ε model (d_B=2.8 mm) and pressure outlet BC in a polyhedral grid, and (f) the SM impeller model with SST k-ω model (d_B=1.8 mm) and pressure outlet BC in a polyhedral grid.

This pushed us to find out whether and how their occurrence was caused or affected by applying different grid types, turbulence models, and bubble sizes. For this purpose, two types of contours were created.

First, the so-called Q-criterion was used to identify areas in the vicinity of the impellers where the vorticity magnitude is greater than the magnitude of the rate of strain. The plots in Fig. 12 show Q-value surfaces with a constant value of 1066.3 s^{-2} coloured by the liquid velocity magnitude. The plots show the single vortex, starting from the outer edge of the blades, the typical location for a pitched blade turbine. The trailing vortices behind the blades are longer for the degassing boundary condition (Fig. 12-a) than in the rest of the cases which all were carried out using a pressure outlet boundary condition. Switching the simulation from MRF to SM (Fig. 12–c and Fig. 12–d) increases the size of the trailing vortex as well as the liquid velocity. Generally, the various cases in which mesh type, turbulence model, and bubble diameter were varied, exhibit vortices of different sizes at each impeller, and vortex sizes which are different at the two impellers.

Secondly, Fig. 13 shows the exact location of the maximum velocity vectors found in each case in the form of an iso-surface coloured by their values. For the degassing boundary condition (Fig. 13–a), the maximum velocity (u_{Max}= 0.97 m/s) shows up at a spot where the impeller is attached to the shaft. However, for the pressure outlet boundary condition (Fig. 13–b), the location of the maximum velocity (u_{Max}= 0.74 m/s) changes to the tip of the bottom impeller. As this shift might be due to a slight difference between the grids in the two cases (the mesh changes after the addition of the air headspace), the shift might not be directly related to an effect of the difference in boundary condition on the (overall) flow field.

For the case (Fig. 13–e) where the SM simulation is carried out on a polyhedral grid, the location of the maximum velocity changes from the impeller tip to the point where the impeller is attached to the shaft, while the maximum velocity increases compared to the mosaic grid of Fig. 13–d. Since the only difference between Fig. 13–d and Fig. 13–e is the mesh type, this submits that both location and magnitude of the spurious velocities depend on grid type and grid resolution. Finally, studying the influence of the turbulence model as well as the bubble diameter showed that the location and the magnitude of the spurious velocity are both changing. Fig. 13–f shows that the location of the maximum liquid velocity is not at the blade attachment point of the bottom impeller, but it moves to the blade-shaft attachment point of the top impeller, while it is slightly smaller for the case of the realizable k-ε.

The variations in both the location of these maximum velocities and their magnitude are a strong indication that

the maximum velocities are spurious indeed. They may be caused by misalignments between curved impeller blades and mesh and/or may be due to numerical issues related to the close proximity of the interface between the zones, the single baffle and the various dip tubes. These misalignments may work out differently for MRF and SM based simulations, for different meshes and for different turbulence models.

6. Conclusions

On the basis of the sensitivity analysis carried out with the help of the commercial flow solver ANSYS/Fluent, several important conclusions are drawn with the view of computationally simulating a fully equipped lab-scale aerated bioreactor. These conclusions particularly relate to the effects of top surface boundary condition, impeller treatment, mesh type and density, turbulence model, and imposed constant bubble diameter:

- A lab-scale (2 L) bioreactor with a (rather) small spacing between impeller and liquid surface and without wall-mounted baffles is prone to the formation of a vortex around the impeller axis which may be a substantial part of the liquid volume. This was investigated in two-fluid simulations using the Multiple Reference Frames (MRF) approach. The conclusion is that a pressure outlet boundary condition at the interface between liquid and air head space should be used to allow for such a central vortex rather than the degassing boundary condition.
- In two-fluid simulations with the air head space, the flow fields calculated by using the steady-state MRF approach look rather similar to snapshots from a simulation obtained by using the dynamic Sliding Mesh (SM) technique, except that the latter exhibit vortical structures in horizontal cross-sections.
- In two-fluid simulations with the air head space, a dynamic SM based simulation is capable of dispersing the gas phase far better than a simulation using the MRF approach while with SM the overall gas fraction is higher and in far better agreement with the experimental value.
- In our two-fluid simulations, using an MRF flow field as the initial condition of an SM based simulation does not prove a good strategy, as the time needed to attain the eventual SM overall gas volume fraction was excessively long.
- In an SM based simulation, a polyhedral mesh outperformed the mosaic grid, and the SST k-ω turbulence model produced better results than the realizable k-ε model.
- In our SM based simulations with low aeration rates, the effects of grid type and turbulence model were much more prominent than the choice of the constant bubble size (1.8 or 2.8 mm). This relates to both velocity magnitudes and air volume fraction.
- Spurious velocities associated with the profiled impeller blades were observed in almost all simulations. Using different meshes (mosaic or polyhedral), applying different meshing strategies, switching from MRF to SM, and using different turbulence models resulted in spurious velocities at different positions on the blades and did not eliminate them completely. Our recommendation is to try and reduce their occurrence but to ignore them eventually, and not to attach significance to the maximum velocities reported by the simulation.

The overall conclusion is that RANS-based two-fluid simulations of aerated lab-scale bioreactors are very sensitive (at least) to the way the revolving impeller is accounted for, to mesh type and mesh density, and to the turbulence model.

Declaration of Competing Interest

The authors declare that they have no known competing financial interests or personal relationships that could have appeared to influence the work reported in this paper.

Acknowledgement

The authors would like to acknowledge financial support from Science Foundation Ireland (SFI) co-funded under the European Regional Development: 12/RC/2275_P2.

References

2022Ansys Fluent Theory Guide.
Ammar, M., Driss, Z., Chtourou, W., Abid, M.S., 2011. Effects of baffle length on turbulent flows generated in stirred vessels. Cent. Eur. J. Eng. 1, 401–412.
Aubin, J., Fletcher, D.F., Xuereb, C., 2004. Modeling turbulent flow in stirred tanks with CFD: the influence of the modeling approach, turbulence model and numerical scheme. Exp. Therm. Fluid Sci. 28, 431–445.
Bach, C., Yang, J., Larsson, H., Stocks, S.M., Gernaey, K.V., Albaek, M.O., Krühne, U., 2017. Evaluation of mixing and mass transfer in a stirred pilot scale bioreactor utilizing CFD. Chem. Eng. Sci. 171, 19–26.
Bujalski, W., Jaworski, Z., Nienow, A., 2002. CFD study of homogenization with dual Rushton turbines—Comparison with experimental results: Part II: The multiple reference frame. Chem. Eng. Res. Des. 80, 97–104.
Cappello, V., Plais, C., Vial, C., Augier, F., 2021. Scale-up of aerated bioreactors: CFD validation and application to the enzyme production by Trichoderma reesei. Chem. Eng. Sci. 229, 116033.
Coroneo, M., Montante, G., Paglianti, A., Magelli, F., 2011. CFD prediction of fluid flow and mixing in stirred tanks: Numerical issues about the RANS simulations. Comput. Chem. Eng. 35, 1959–1968.
Deglon, D.A., Meyer, C.J., 2006. CFD modelling of stirred tanks: Numerical considerations. Miner. Eng. 19, 1059–1068.
Dhotre, M., Deen, N., Niceno, B., Khan, Z., Joshi, J., 2013. Large eddy simulation for dispersed bubbly flows: a review. Int. J. Chem. Eng. 2013.
Gelves, R., Dietrich, A., Takors, R., 2014. Modeling of gas–liquid mass transfer in a stirred tank bioreactor agitated by a Rushton turbine or a new pitched blade impeller. Bioprocess Biosyst. Eng. 37, 365–375.
Gentric, C., Mignon, D., Bousquet, J., Tanguy, P., 2005. Comparison of mixing in two industrial gas–liquid reactors using CFD simulations. Chem. Eng. Sci. 60, 2253–2272.
Giacomelli, J.J., Van den Akker, H.E., 2020. Correction to: Time Scales and Turbulent Spectra above the Base of Stirred Vessels from Large Eddy Simulations. Flow., Turbul. Combust. 105, 63–66.
Günyol, Ö., 2017. Computational fluid dynamics of gassed-stirred fermenters. University of Delft.
Haringa, C., 2017. Through the Organism's eyes: The interaction between hydrodynamics and metabolic dynamics in industrial-scale fermentation processes. University of Delft.
Haringa, C., Vandewijer, R., Mudde, R.F., 2018a. Inter-compartment interaction in multi-impeller mixing. Part II. Experiments, sliding mesh and large Eddy simulations. Chem. Eng. Res. Des. 136, 886–899.
Haringa, C., Vandewijer, R., Mudde, R.F., 2018b. Inter-compartment interaction in multi-impeller mixing: Part I. Experiments and multiple reference frame CFD. Chem. Eng. Res. Des. 136, 870–885.
Hartmann, H., Derksen, J., Montavon, C., Pearson, J., Hamill, I., Van den Akker, H., 2004. Assessment of large eddy and RANS stirred tank simulations by means of LDA. Chem. Eng. Sci. 59, 2419–2432.
Hinze, J., 1975. Turbulence. McGraw-Hill, New York.

Jaworski, Z., Bujalski, W., Otomo, N., Nienow, A., 2000. CFD study of homogenization with dual rushton turbines—Comparison with experimental results: Part I: Initial studies. Chem. Eng. Res. Des. 78, 327–333.
Joshi, J.B., Nere, N.K., Rane, C.V., Murthy, B., Mathpati, C.S., Patwardhan, A.W., Ranade, V.V., 2011a. CFD simulation of stirred tanks: Comparison of turbulence models (Part II: Axial flow impellers, multiple impellers and multiphase dispersions). Can. J. Chem. Eng. 89, 754–816.
Joshi, J.B., Nere, N.K., Rane, C.V., Murthy, B., Mathpati, C.S., Patwardhan, A.W., Ranade, V.V., 2011b. CFD simulation of stirred tanks: Comparison of turbulence models. Part I: Radial flow impellers. The. Can. J. Chem. Eng. 89, 23–82.
Karimi, M., Akdogan, G., Bradshaw, S.M., 2012a. Effects of different mesh schemes and turbulence models in CFD modelling of stirred tanks. Physicochem. Probl. Miner. Process. 48.
Karimi, M., Akdogan, G., Dellimore, K.H., Bradshaw, S.M., 2012b. Quantification of numerical and model uncertainties in the CFD simulation of the gas holdup and flow dynamics in a laboratory scale Rushton-turbine flotation tank, the 9th International Conference on CFD in the Minerals and Process Industries.
Kerdouss, F., Bannari, A., Proulx, P., 2006. CFD modeling of gas dispersion and bubble size in a double turbine stirred tank. Chem. Eng. Sci. 61, 3313–3322.
Kerdouss, F., Bannari, A., Proulx, P., Bannari, R., Skrga, M., Labrecque, Y., 2008. Two-phase mass transfer coefficient prediction in stirred vessel with a CFD model. Comput. Chem. Eng. 32, 1943–1955.
Koh, P., Schwarz, M., 2006. CFD modelling of bubble–particle attachments in flotation cells. Miner. Eng. 19, 619–626.
Koh, P., Schwarz, M., Zhu, Y., Bourke, P., Peaker, R., Franzidis, J., 2003. Development of CFD models of mineral flotation cells, Third International Conference on Computational Fluid Dynamics in the Minerals and Process Industries, Melbourne, Australia, pp. 171–175.
Kuschel, M., Fitschen, J., Hoffmann, M., von Kameke, A., Schlüter, M., Wucherpfennig, T., 2021. Validation of novel lattice Boltzmann Large Eddy Simulations (LB LES) for equipment characterization in biopharma. Processes 9, 950.
Lane, G., 2015. Predicting the energy dissipation rate in a mechanically stirred tank, Eleventh International Conference on CFD in the Minerals and Process Industries. CSIRO Australia Melbourne, Australia.
Lane, G., Schwarz, M., Evans, G., 2000a. Comparison of CFD methods for modelling of stirred tanks, 10th European Conference on Mixing. Elsevier, pp. 273–280.
Lane, G., Schwarz, M., Evans, G., 2000b. Modelling of the interaction between gas and liquid in stirred vessels, 10th European Conference on Mixing. Elsevier, pp. 197–204.
Lane, G., Schwarz, M., Evans, G., 2002. Predicting gas–liquid flow in a mechanically stirred tank. Appl. Math. Model. 26, 223–235.
Li, X., Scott, K., Kelly, W.J., Huang, Z., 2018. Development of a computational fluid dynamics model for scaling-up Ambr bioreactors. Biotechnol. Bioprocess Eng. 23, 710–725.
Luo, J., 1994. Prediction of impeller induced flows in mixing vessels using multiple frames of reference, I. Chem. E. Symposium Series, pp. 549–556.
Menter, F.R., 1994. Two-equation eddy-viscosity turbulence models for engineering applications. AIAA J. 32, 1598–1605.
Montante, G., Bakker, A., Paglianti, A., Magelli, F., 2006. Effect of the shaft eccentricity on the hydrodynamics of unbaffled stirred tanks. Chem. Eng. Sci. 61, 2807–2814.
Montante, G., Lee, K., Brucato, A., Yianneskis, M., 2001. Numerical simulations of the dependency of flow pattern on impeller clearance in stirred vessels. Chem. Eng. Sci. 56, 3751–3770.
Montante, G., Paglianti, A., Magelli, F., 2007. Experimental analysis and computational modelling of gas–liquid stirred vessels. Chem. Eng. Res. Des. 85, 647–653.
Newell, R., Grano, S., 2007. Hydrodynamics and scale up in Rushton turbine flotation cells: Part 1—Cell hydrodynamics. Int. J. Miner. Process. 81, 224–236.
Ng, K., Fentiman, N., Lee, K., Yianneskis, M., 1998. Assessment of sliding mesh CFD predictions and LDA measurements of the flow in a tank stirred by a Rushton impeller. Chem. Eng. Res. Des. 76, 737–747.
Nienow, A.W., 2006. Reactor engineering in large scale animal cell culture. Cytotechnology 50, 9.
Nienow, A.W., Rielly, C.D., Brosnan, K., Bargh, N., Lee, K., Coopman, K., Hewitt, C.J., 2013. The physical characterisation of a microscale parallel bioreactor platform with an industrial CHO cell line expressing an IgG4. Biochem. Eng. J. 76, 25–36.
Oshinowo, L., Jaworski, Z., Dyster, K.N., Marshall, E., Nienow, A. W., 2000. Predicting the tangential velocity field in stirred tanks using the Multiple Reference Frames (MRF) model with validation by LDA measurements, 10th European conference on mixing. Elsevier, pp. 281–288.
Rafiq, Q.A., Brosnan, K.M., Coopman, K., Nienow, A.W., Hewitt, C.J., 2013. Culture of human mesenchymal stem cells on microcarriers in a 5 l stirred-tank bioreactor. Biotechnol. Lett. 35, 1233–1245.
Rotondi, M., Grace, N., Betts, J., Bargh, N., Costariol, E., Zoro, B., Hewitt, C.J., Nienow, A.W., Rafiq, Q.A., 2021. Design and development of a new ambr250® bioreactor vessel for improved cell and gene therapy applications. Biotechnol. Lett. 43, 1103–1116.
Sadino-Riquelme, M.C., Rivas, J., Jeison, D., Donoso-Bravo, A., Hayes, R.E., 2022. Computational modelling of mixing tanks for bioprocesses: Developing a comprehensive workflow. The. Can. J. Chem. Eng. 100, 3210–3226.
Sajjadi, B., Raman, A.A.A., Ibrahim, S., Shah, R.S.S.R.E., 2012. Review on gas-liquid mixing analysis in multiscale stirred vessel using CFD. Rev. Chem. Eng. 28, 171–189. https://doi.org/10.1515/revce-2012-0003
Sanyal, J., Vásquez, S., Roy, S., Dudukovic, M., 1999. Numerical simulation of gas–liquid dynamics in cylindrical bubble column reactors. Chem. Eng. Sci. 54, 5071–5083.
Scargiali, F., D'Orazio, A., Grisafi, F., Brucato, A., 2007. Modelling and simulation of gas–liquid hydrodynamics in mechanically stirred tanks. Chem. Eng. Res. Des. 85, 637–646.
Schubert, H., 1986. On the hydrodynamics and the scale-up of flotation processes, Advances in mineral processing: A half century of progress in application of theory and practive.
Shi, P., Rzehak, R., 2018. Bubbly flow in stirred tanks: Euler-Euler/RANS modeling. Chem. Eng. Sci. 190, 419–435.
Thomas, J.A., Liu, X., DeVincentis, B., Hua, H., Yao, G., Borys, M.C., Aron, K., Pendse, G., 2021. A mechanistic approach for predicting mass transfer in bioreactors. Chem. Eng. Sci. 237, 116538.
Van den Akker, H.E., 2006. The details of turbulent mixing process and their simulation. Adv. Chem. Eng. 31, 151–229.
Van den Akker, H.E., 2015. Mesoscale flow structures and fluid–-particle interactions. Adv. Chem. Eng. 46, 281–354.
Venneker, B.C., Derksen, J.J., Van den Akker, H.E., 2002. Population balance modeling of aerated stirred vessels based on CFD. AIChE J. 48, 673–685.
Yeoh, S., Papadakis, G., Yianneskis, M., 2004. Numerical simulation of turbulent flow characteristics in a stirred vessel using the LES and RANS approaches with the sliding/deforming mesh methodology. Chem. Eng. Res. Des. 82, 834–848.